

POLITECNICO
MILANO 1863

SCUOLA DI INGEGNERIA INDUSTRIALE
E DELL'INFORMAZIONE

Enhancing Transonic Airfoil Efficiency Through Localized Friction Reduction

Tesi di Laurea Magistrale in
Aeronautical Engineering - Ingegneria Aeronautica

Davide Alloggio, 259066

Advisor:
Prof. Maurizio Quadrio

Co-advisors:
Prof. Alessandro Chiarini
Niccolò Berizzi

Academic year:
2025-2026

Abstract: The effect of riblet positioning on a transonic airfoil is investigated. A parametric RANS study is performed to assess the sensitivity of the airfoil performance, expressed through the lift-to-drag ratio, to the position of application of the control. The effect of locally optimal riblets is modelled in RANS by enforcing a properly defined partial slip boundary condition for velocity. Consistent with previous works, riblet presence is confirmed to reduce the skin friction and to modify the flow features by moving the shock towards the trailing edge. The suction side exhibits the highest sensitivity to the control application. The best-performing configurations are those situated in the front section, which induce the most significant alterations to the global flow features. The analysis performed at two different Reynolds numbers demonstrates a reduction in riblet effectiveness as the Reynolds number increases. At $\mathrm{Re}_\infty = 3 \cdot 10^5$, the profile entirely covered by riblets features $\Delta E = +7.4\%$ and the partial coverage configuration with the best performance achieves $\Delta E = +1.9\%$. These values diminish to $\Delta E = +4.0\%$ for the fully covered profile and $\Delta E = +1.7\%$ for the optimal partial coverage configuration at $\mathrm{Re}_\infty = 10^6$. The adjoint equations to obtain the sensitivity of the aerodynamic efficiency to the application of a slip velocity at the wall are derived, establishing the theoretical framework for a fully automated optimization process.

Key-words: RANS, Skin Friction Reduction, Transonic Flows

1. Introduction

The fast depletion of natural resources and the increase of atmospheric pollution require a shift towards sustainable solutions in every aspect of human life. Civil aviation alone accounts for 2.4 % of global CO_2 emissions (Klöwer *et al.*, 2021) and ICAO estimates the environmental pollution due to air transport to triple by 2050 (Graver *et al.*, 2019). In this context, the development of more efficient aircraft is becoming mandatory to reduce fuel consumption and, therefore, both emissions and operational costs. From an aerodynamic perspective, this necessity translates into the development of reliable solutions capable of improving performance in terms of flow-induced forces. Hence, the study of drag reduction techniques is becoming of great interest in order to satisfy this requirement and contribute to a more sustainable aviation industry.
Drag reduction devices are divided into active and passive ones (Gad-el-Hak, 2000). Active controls lead to high drag reduction, but require energy for the actuation to function. In order to correctly assess the performance of these techniques, it is necessary to consider the balance between energy savings and the consumption of

the control system. Passive controls are capable of manipulating the flow characteristics only through their application and, despite their lower absolute drag reduction, are simpler and do not add mechanical complexity due to energy requirements. Riblets (García-Mayoral & Jiménez, 2011) are one of the most promising solutions among passive drag reduction systems, consisting of streamwise-aligned grooves with sharp tips and dimensions comparable to the viscous sublayer, which reduce skin friction at the point of application.

The study of skin friction reduction through riblets as a possible application in aeronautics started at NASA as a consequence of the energy crisis in the second half of the 1970s (Walsh, 1980; Walsh & Weinstein, 1979), and continued with the studies performed in the Berlin oil tunnel by Bechert *et al.* (1997). They tested various riblet configurations on a flat plate assessing the importance of riblet spacing and height, obtaining a drag reduction of 6-8% for riblet shapes suitable for aircraft applications.

Theoretical studies of the physical mechanisms underpinning the drag reduction capabilities of riblets were initially performed by Bechert & Bartenwerfer (1989) who defined the protrusion height ($h_{||}$) as the distance between the riblet tip and the virtual origin of the equivalent flat plate that generates the same velocity profile, and computed it for a number of riblet shapes. The theoretical understanding of the functioning of riblets was proposed by Luchini *et al.* (1991), who defined the protrusion height for the cross flow ($h_{\perp}$), showing how the riblet effect depends only on $\Delta h = h_{||} - h_{\perp}$ and proving it to be equivalent to the slip length λ, the quantity that linearly relates the velocity at the wall with the shear rate (Maxwell, 1879; Navier, 1823). Riblets offer more resistance to the cross flow than to the streamwise one; this causes the turbulent structures near the wall to be pushed further from it, reducing the momentum mixing and consequently the skin friction. Later on, the same author (Luchini, 1996) described this effect as equivalent to an upward shift of the logarithmic velocity profile by a quantity Δh, which has a direct impact on the friction coefficient. Later, Gómez-de-Segura *et al.* (2018) showed through Direct Numerical Simulations (DNS) that the slip length in wall units λ^+ corresponds to the upward shift of the velocity profile ΔU^+. The superscript $+$ indicates a quantity non-dimensionalized with viscous units, $\lambda^+ = \lambda u_\tau/\nu$ and $\Delta U^+ = \Delta U/u_\tau$ where ν is the kinematic viscosity, $u_\tau = \sqrt{\tau_w/\rho}$ is the friction velocity, τ_w is the local shear stress and ρ is the density.

After the drag reduction potential of riblets on a flat surface had been assessed, experimental campaigns highlighted their increased efficiency in the presence of moderate pressure gradients, such as on airfoils at mild incidence (Debisschop & Nieuwstadt, 1996; Sundaram *et al.*, 1996). Further studies on 3D wings and flight tests confirmed those results as long as the riblet orientation is within 10° of the direction of the flow on the wing (Szodruch, 1991; Viswanath, 2002), proving the applicability of riblets on long-range aircraft.

Both experiments and numerical simulations agree that riblet performance is directly dependent on their dimensions and shape. García-Mayoral & Jiménez (2011) noticed that, defining A_g as the cross-sectional area of the groove, drag reduction data for various types of riblets collapse better if considered against the parameter $l_g^+ = \sqrt{A_g^+}$ which is influenced by both the riblet height and the groove shape. They obtained optimal performance for $l_g^+ \approx 10.5$ which corresponds, as also reported in other studies (Mele & Tognaccini, 2018; Walsh, 1980), to an upward shift of the logarithmic velocity profile by one viscous unit ($\Delta U^+ = 1$).

The study of riblets in aeronautical applications is inherently connected with their representation in numerical simulations. While it is possible to directly model riblets or their effect on near-wall turbulence using DNS (Garcia-Mayoral & Jiménez, 2011; Gómez-de-Segura *et al.*, 2018) and Large Eddy Simulations (LES), those types of simulations are unfeasible in the final cases of interest. The standard approach in the study and design of high-Reynolds applications is the usage of Reynolds-Averaged Navier-Stokes Equations (RANS). Due to the low resolution level and the approximation of turbulence that characterize them, RANS models are not able to directly represent riblets. In order to implement drag reduction by riblets in RANS, Mele and Tognaccini (Mele & Tognaccini, 2012; Mele *et al.*, 2016) proposed a modified boundary condition for the $k-\omega$ SST turbulence model developed to take into account the presence of riblets on the wall through the introduction of appropriate coefficients to the Wilcox boundary condition for ω (Wilcox, 2006). Aupoix *et al.* (2012) conducted similar work for the SA turbulence model, continued by Koepplin *et al.* (2017) who extended the model for compressible turbomachinery applications.

Since the previous method based on the modification of the value at the wall of ω in the $k-\omega$ SST model fails in correctly representing devices that cause higher drag reduction than riblets, Mele & Tognaccini (2018) developed a new velocity boundary condition based on the slip length concept. This new formulation allows the representation of any skin friction reduction technique that can be characterized by an equivalent slip length. They found that in both incompressible and transonic configurations, in addition to reducing the skin friction drag, riblet application on an airfoil alters the pressure distribution causing the lift to increase; this is translated into a lift-to-drag ratio improvement. Cacciatori *et al.* (2022) used the same boundary condition and confirmed these results in the incompressible regime, studying the effect of riblets on both a NACA 0012 profile and a UAV. The same authors highlighted also that riblets show a different level of effectiveness in relation to the point of application and the corresponding flow conditions. They concluded that in a full body configuration it is preferable, from a cost-benefit point of view, to apply riblets only on the parts of the wing more sensitive to their presence rather than applying them on all the available surface.

Further studies on drag reduction over a transonic airfoil were performed by Quadrio *et al.* (2022), who studied through DNS the effect of spanwise forcing (Quadrio *et al.*, 2009) applied on the suction side of a V2C supercritical airfoil. This active control technique involves the application of a space- and time-dependent spanwise velocity distribution, which interacts with the near-wall turbulence and, correctly tuning the parameters, reduces skin friction. They showed that the controlled case exhibits a more intense shock wave shifted towards the trailing edge, which causes a pressure drag increase coupled with a lift enhancement. In order to keep the lift constant, as in cruise conditions, it is possible to reduce the angle of attack. In this modified condition, the authors computed a drag reduction of 15% with respect to the uncontrolled case, estimated to be 9% if extended from the airfoil alone to the full aircraft configuration. The authors suggested that the results can be valuable also in the description of other skin friction reduction techniques, such as riblets. Later studies by Berizzi *et al.* (2025) investigated the drag reduction in the same configuration by varying different parameters of the control to find the best combination in the examined case. In the same work, the physics of the control was studied in detail, quantifying the pressure and friction drag variation caused by the actuation and confirming the effectiveness of spanwise forcing for total drag reduction as described by Quadrio *et al.* (2022). The authors also performed a boundary layer evaluation, highlighting how the friction reduction device modifies its characteristics. The control reduces the momentum deficit up to the shock location but makes the boundary layer more prone to reversal immediately after it.
While the fundamental physics of skin friction reduction have been extensively detailed in previous literature, this research shifts the focus toward application and optimization. To the author's best knowledge, an optimization study regarding the placement of skin friction reduction devices in transonic conditions has not yet been performed. Therefore, this thesis aims to lay the groundwork for such an investigation. A slip length boundary condition for optimal riblet modelling is implemented and validated in standard incompressible cases and then applied to an airfoil in transonic conditions at two different Reynolds numbers, investigating the dependency between the point of application and the variation in lift-to-drag ratio. Despite the inherent limitations of a discrete parametric study and RANS simulations, the primary objective is to identify the optimal regions for applying these devices to maximize overall aerodynamic performance. Since riblet effectiveness is sensitive to local flow conditions and their operational cost is directly linked to the portion of the ribbed surface, knowing the locations where riblets produce the highest benefits is of paramount importance. To support this goal, a reliable open-source environment has been developed in order to model riblets in both compressible and incompressible cases. This computational setup has been employed to conduct an evaluation of the impact of riblet positioning on the performance of a supercritical airfoil. Furthermore, the adjoint equations needed for a gradient-based optimization of the riblet locations are derived. This work is structured as follows: Section 2 describes the numerical methods and the investigated space of parameters; Section 3 contains the results regarding the riblet application on the supercritical airfoil and the impact of their placement; Section 4 proposes a critical interpretation of the results; Section 5 contains the adjoint equations and the corresponding boundary conditions; Section 6 includes the conclusions.

2. Methods

2.1. Governing Equations

In this work, riblet performance is assessed by solving the RANS equations (Eq.1). These are derived from the Navier-Stokes conservation equations by taking the time average after splitting the velocity field into its time-averaged component and its fluctuating one. The resulting terms requiring closure are the Reynolds Stresses, denoted as $\left(\overline{\boldsymbol{u}' \cdot \boldsymbol{u}'}\right)$, where the overbar $\overline{(\cdot)}$ represents the time average operator and $\boldsymbol{u}'$ indicates the fluctuating component of the velocity. The modelling of this term is handled by a turbulence model under the Boussinesq hypothesis which assumes that it is proportional to the symmetric part of the velocity gradient through the turbulent viscosity ν_t. The latter is computed by solving one or more Partial Differential Equations (PDEs), containing coefficients properly tuned to correctly represent the turbulence contribution to the mean flow.
Enforcing the hypothesis of steady flow and negligible body forces, the formulation of the governing equations is the following:

$$\begin{aligned} &\nabla \cdot (\rho \boldsymbol{u}) = 0 \\ &\nabla \cdot (\rho \boldsymbol{u} \otimes \boldsymbol{u}) + \nabla p - \nabla \cdot \boldsymbol{\tau} = 0 \\ &\nabla \cdot (\rho \boldsymbol{u} E_t) + \nabla \cdot (p \boldsymbol{u}) - \nabla \cdot (\boldsymbol{\tau} \cdot \boldsymbol{u}) - \nabla \cdot \boldsymbol{q} = 0 \end{aligned} \tag{1}$$

where ρ is the density, $\boldsymbol{u}$ is the time-averaged component of the velocity field, p is the static pressure, $E_t = e + \frac{1}{2}|\boldsymbol{u}|^2$ is the total energy, $\boldsymbol{q}$ is the heat flux and $\boldsymbol{\tau}$ is the viscous stress tensor:

$$\boldsymbol{\tau} = \rho \nu_{eff} \left(\nabla \boldsymbol{u} + (\nabla \boldsymbol{u})^T - \frac{2}{3} (\nabla \cdot \boldsymbol{u}) \boldsymbol{I} \right) \tag{2}$$

where ν_{eff} is the effective viscosity and contains the effect of the turbulence model:

$$\nu_{eff} = \nu + \nu_t \tag{3}$$

The use of a turbulence model allows the representation of the effect of turbulent structures on the mean flow without computing the velocity fluctuations, keeping the computational cost and mesh requirements manageable. This advantage comes with the limitation of a less accurate representation of the physics of the problem. These characteristics make RANS simulations a powerful tool to compute global forces in complex configurations but they lack the ability to describe the turbulent phenomena that take place in the boundary layer.
The results presented here are obtained by solving the RANS equations in both compressible and incompressible cases using OpenFOAM (Weller *et al.*, 1998), a widely used publicly available CFD environment that discretizes the equations and solves them using a finite volume method. Its open-source nature allows a straightforward customization of the code, a characteristic of paramount importance for the development of the present study.

2.2. Slip Length Boundary Condition

Luchini (1996) showed that the reduced scale of riblets allows the representation of their local effect, which consists of altering the distance of the turbulent structures from the wall, as a homogeneous vertical shift ΔU^+ of the logarithmic portion of the turbulent velocity profile:

$$U^+ = \frac{1}{\kappa}\ln(y^+) + A + \Delta U^+ \tag{4}$$

where $A = 4.48$ is the intercept for smooth walls and $\kappa = 0.392$ is the von Kármán constant. The values of both quantities are reported following the results obtained by the same author in a later work (Luchini, 2017). However, given that the present study investigates relative performance variations, the specific choice of these constants does not alter the final outcomes.
As described by Mele & Tognaccini (2018), it is possible to shift the velocity profile by a quantity ΔU^+ through the imposition of an appropriate slip length λ at the wall. The slip length definition linearly relates the slip velocity, here denoted as $\boldsymbol{u}_w$, to the shear rate at the wall:

$$\boldsymbol{u}_w = \lambda \left(\frac{\partial \boldsymbol{u}}{\partial \boldsymbol{n}}\right)_w \tag{5}$$

the quantity $\boldsymbol{n}$ is the unit vector normal to the surface.
In this work the riblet effect is modelled by implementing a boundary condition that imposes a slip velocity at the wall according to Eq. (5). In a discrete solver the implementation requires a discrete formulation, by approximating the wall-normal derivative with finite differences, it is possible to write:

$$\boldsymbol{u}_w = \lambda \frac{\boldsymbol{u}_1 - \boldsymbol{u}_w}{d} \tag{6}$$

where $\boldsymbol{u}_1$ is the velocity evaluated at the centre of the first cell adjacent to the wall and d is the distance between it and the wall. Rearranging:

$$\boldsymbol{u}_w = \boldsymbol{u}_1 \frac{\lambda}{\lambda + d} \tag{7}$$

The results obtained by Gómez-de-Segura *et al.* (2018), who showed that the upward shift of the velocity profile corresponds to the slip length if both are expressed in wall units, are exploited:

$$\lambda^+ = \Delta U^+ \tag{8}$$

The dimensionless value of the slip length is linked to the dimensional counterpart through the following relation:

$$\lambda^+ = \lambda \frac{u_\tau}{\nu} \tag{9}$$

The application of a slip length boundary condition which sets the value of λ^+ allows the user to impose a fixed shift of the velocity profile. The presented results are obtained by imposing $\lambda^+ = \Delta U^+ = 1$ at each point of application of the constraint, corresponding to the maximum achievable with riblets (García-Mayoral & Jiménez, 2011). This is equivalent to the application of locally optimal riblets, whose height changes with the application point to maximize the skin friction drag reduction effect. A boundary condition structured in this way allows not only the representation of optimal riblets but, by changing the value of the imposed slip length, also the extension of this approach to any drag-reducing surface treatment, provided an equivalent slip length can be defined.

After its implementation, the boundary condition is validated against well-characterized incompressible test cases, namely a flat plate and a NACA 0012 at varying incidence. The effects of riblets on a NACA 0012 with an angle of attack $\alpha = 4°$ are reported in Figure 1. The velocity profile clearly shows how the implemented numerical setup effectively imposes a unitary shift to the velocity profile. This is confirmed by the fact that the controlled velocity profile overlaps the uncontrolled one if rigidly downshifted by its wall value. Although the friction coefficient exhibits minor discrepancies at the transition location with respect to the validation data, the baseline distribution is well represented. More importantly, the numerical setup correctly captures the riblet-induced downward shift of the C_f curve, confirming the expected skin friction reduction in agreement with previous works.
The full validation process for both the boundary condition and the compressible environment, together with the computational setup used to perform such simulations, are reported in Appendix A.

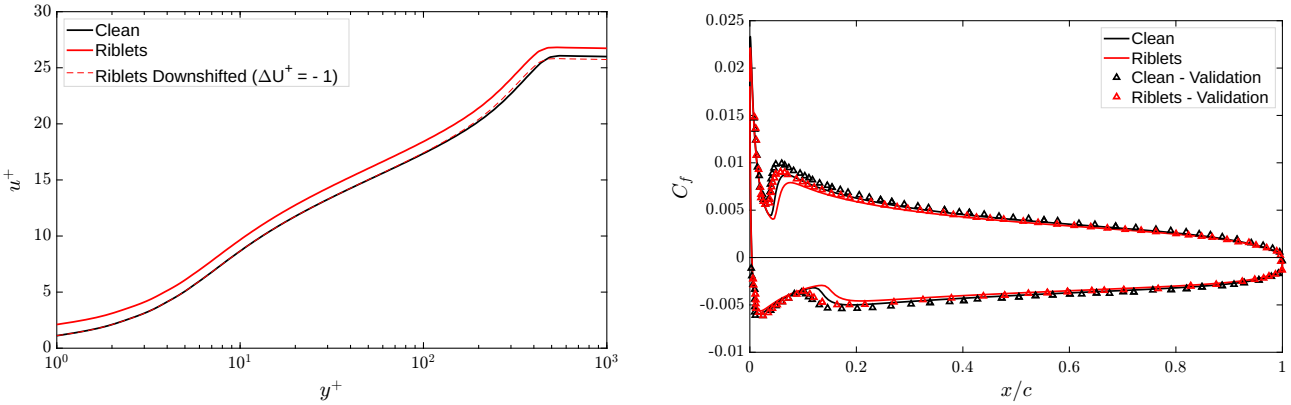

Figure 1: Velocity profile extracted at $x/c = 0.5$ (left) and friction coefficient evolution (right) on the NACA 0012 airfoil for $\alpha = 4°$ validated against the results obtained by Mele & Tognaccini (2012).

2.3. Forces and Coefficients

The evaluation of riblet effectiveness is performed through their influence on the overall airfoil performance. Aerodynamic loads are directly dependent on the pressure and the friction distribution along the airfoil, which can be quantified through the pressure and the friction coefficient:

$$\begin{aligned} C_p(x) &= \frac{p_w(x) - p_\infty}{\frac{1}{2}\rho U_\infty^2} \\ C_f(x) &= \frac{\tau_w(x)}{\frac{1}{2}\rho U_\infty^2} \end{aligned} \tag{10}$$

where τ_w is the shear stress evaluated at the wall, p_w is the pressure at the wall and p_∞ is the freestream pressure.
The aerodynamic force $\mathbf{F}$ is defined integrating along the airfoil the sum of the pressure contribution, acting orthogonally to the wall, and the friction contribution, acting tangentially to it:

$$\mathbf{F} = \int_{S_a} \tau_w \boldsymbol{t}\, \mathrm{d}S - \int_{S_a} p_w \boldsymbol{n}\, \mathrm{d}S \tag{11}$$

where S_a is the airfoil surface, $\boldsymbol{t}$ is the unit tangential vector and $\boldsymbol{n}$ is the outward-pointing unit normal vector with respect to S_a.
The aerodynamic force can be divided into its components orthogonal (Lift) and parallel (Drag) to the freestream direction:

$$\begin{aligned} D &= \mathbf{F} \cdot \hat{\boldsymbol{i}} \\ L &= \mathbf{F} \cdot \hat{\boldsymbol{j}} \end{aligned} \tag{12}$$

in which $\hat{\boldsymbol{i}}$ is the unit vector defining the freestream direction and $\hat{\boldsymbol{j}}$ defines the direction orthogonal to it. The aerodynamic loads can be expressed in dimensionless form using the airfoil chord c as the reference length:

$$\begin{aligned} C_D &= \frac{D}{\frac{1}{2}\rho c U_\infty^2} \\ C_L &= \frac{L}{\frac{1}{2}\rho c U_\infty^2} \end{aligned} \tag{13}$$

2.4. Parameter Space

The main objective of this study is to determine the position in which riblets produce the greatest benefit in terms of performance enhancement on a transonic airfoil. The chosen geometry is the V2C supercritical airfoil developed in the context of the TFAST project (Doerffer *et al.*, 2021) in transonic conditions. A series of RANS simulations are performed, each featuring a patch of length $0.2c$ in a different location where the boundary condition described in this section is applied. The effect of riblet positioning on the performance is assessed in terms of variation of global quantities, represented by the coefficients expressed in Eq. (13) and the lift-to-drag ratio, with respect to the uncontrolled case. Since it has been proven (Mele & Tognaccini, 2018) that riblets affect both lift and drag simultaneously with variations of the same order of magnitude, the lift-to-drag ratio E:

$$E = \frac{L}{D} \tag{14}$$

is the chosen variable to quantify the performance variations between the considered cases. This quantity incorporates both the effect of lift increase and drag reduction, allowing the derivation of the sensitivity without considering multiple parameters. While drag reduction is directly linked to net fuel savings, the lift increase can also be exploited to obtain operational advantages. If flight conditions are kept unchanged, it is possible to maintain the required lift by reducing the angle of attack, which further reduces drag. The lift excess can also be exploited to increase the cruise altitude, where the lower freestream density reduces total drag, or to increase the payload capacity.
The complete set of investigated configurations, obtained by systematically varying the patch location, is summarized in Table 1. Each case identifier specifies the targeted surface, either the suction side (SS) or the pressure side (PS), followed by the normalized coordinate of the patch center. The Baseline case indicates the simulation of the clean airfoil, while in the Full Coverage case the simulation is performed applying the boundary condition to all the airfoil surface. These two cases serve as reference boundaries for the uncontrolled configuration and the maximum benefit achievable, allowing for a comprehensive evaluation of the benefits and limitations of each partial configuration.

Table 1: Simulation parameters: each simulation performed is reported defining the patch location and the corresponding ID. x_s defines the patch starting point and x_e the patch ending point

Case ID	x_s/c	x_e/c
Baseline	-	-
SS0.1	0.0	0.2
SS0.2	0.1	0.3
SS0.3	0.2	0.4
SS0.4	0.3	0.5
SS0.5	0.4	0.6
SS0.6	0.5	0.7
SS0.7	0.6	0.8
SS0.8	0.7	0.9
SS0.9	0.8	1.0
PS0.1	0.0	0.2
PS0.3	0.2	0.4
PS0.5	0.4	0.6
PS0.7	0.6	0.8
PS0.9	0.8	1.0
Full Coverage	-	-

3. Results

The effect of riblets on a transonic airfoil is studied for the V2C profile at $\alpha = 4°$ and $\mathrm{Ma}_\infty = 0.7$. The simulations described in Table 1 are performed at two different freestream Reynolds numbers: $\mathrm{Re}_\infty = 3 \cdot 10^5$, which is the validation configuration, and $\mathrm{Re}_\infty = 10^6$. This choice is made to overcome two main limitations of the low-Reynolds-number test case. The first concerns its general applicability: the former freestream Reynolds number is significantly lower than the operational value characterizing real-world flight conditions of a transonic

airfoil at $\mathrm{Ma}_\infty = 0.7$, which for the V2C profile is $\mathrm{Re}_\infty = 3 \cdot 10^6$. The second limitation involves the physical consistency of the numerical model. Since riblets interact with near-wall vortices, they reduce skin friction only within a turbulent boundary layer; the velocity shift described by Luchini (1996) is limited to the logarithmic portion of the velocity profile. In contrast, the implemented boundary condition operates regardless of the local boundary layer state, even when a logarithmic profile is not present. At $\mathrm{Re}_\infty = 10^6$, the freestream conditions are closer to the target values and, as shown by the turbulent kinetic energy distributions displayed in Figure 2, the boundary layer exhibits an earlier transition, extending its turbulent portion and ensuring a more physically consistent analysis.

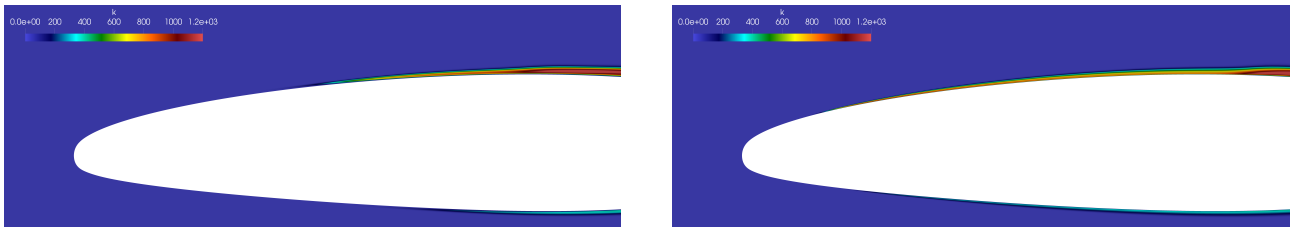

Figure 2: Comparison of the turbulent kinetic energy distribution for the Baseline cases at $\mathrm{Re}_\infty = 3{\cdot}10^5$ (left) and $\mathrm{Re}_\infty = 10^6$ (right)

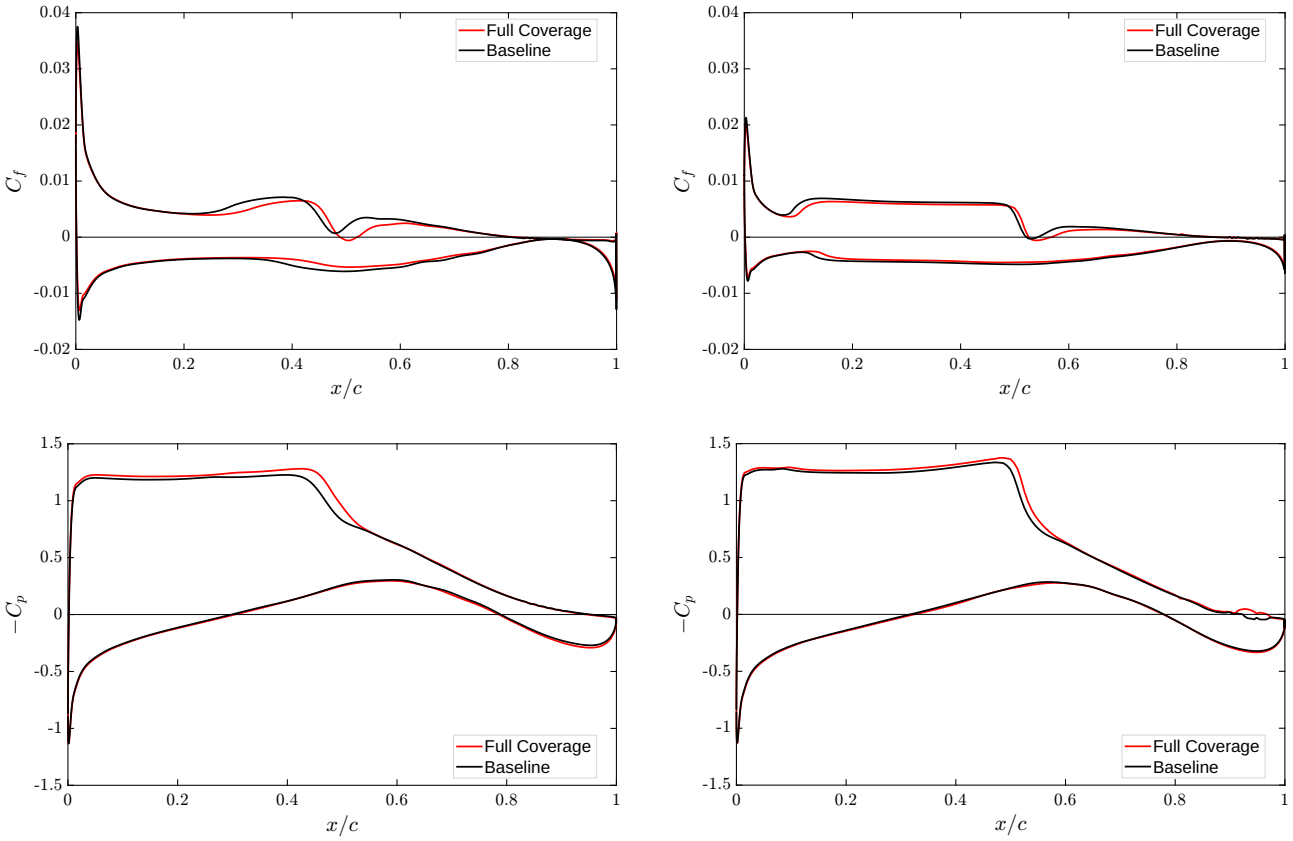

Figure 3: Comparison between Baseline configuration and Full Coverage configuration expressed in terms of C_f distribution (top) and C_p distribution (bottom). Left panels represent quantities evaluated at $\mathrm{Re}_\infty = 3 \cdot 10^5$ while the right panels correspond to $\mathrm{Re}_\infty = 10^6$

First, the V2C airfoil fully covered by locally optimal riblets (named Full Coverage), defined by imposing $\Delta U^+ = 1$, is considered. Figure 3 compares the Baseline case and the completely controlled one in terms of pressure and friction distribution. The C_f distribution confirms that, also in the transonic case, riblet application reduces the skin friction in the point of application. As indicated by the sudden jump in the C_p distribution on the suction side, the application of riblets causes the shock wave to move downstream. Conversely, the C_p distribution on the pressure side remains virtually unaltered, demonstrating that the pressure field modifications are strictly driven by the shock wave dynamics on the suction side. The changes in the flow features induced by the riblet application can be easily visualized drawing the Mach isolines for Ma = 1. Figure 4 confirms the

shock displacement towards the trailing edge, it is also possible to notice an increase in size of the supersonic area over the suction side of the airfoil. The flow in the forward part of the suction side features a stronger acceleration, reducing the pressure which causes the lift to increase. Since supercritical airfoils are designed to delay as much as possible the pressure recovery, the shift of the shock wave towards the trailing edge extends the low-pressure zone on the suction side, leading to a strong increase in the overall lift coefficient.

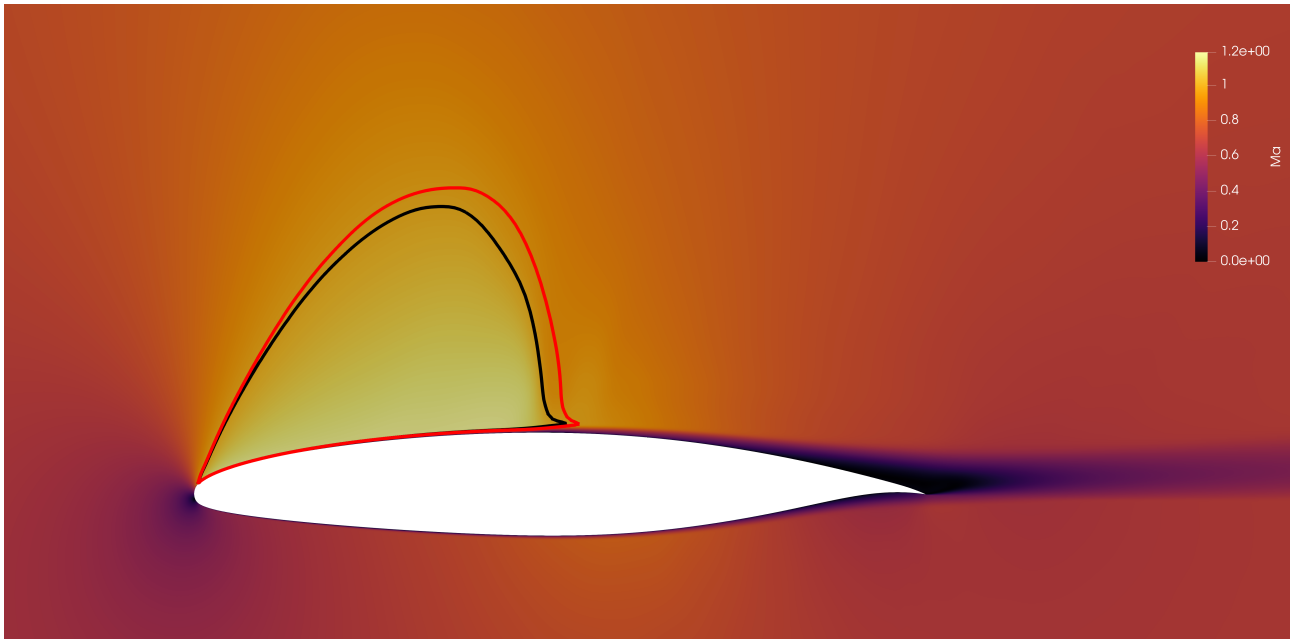

Figure 4: Mach field for the Baseline configuration at $\mathrm{Re}_\infty = 3 \cdot 10^5$ where the Mach isolines for $\mathrm{Ma} = 1$ are reported (black line). Overlaid is the unitary Mach isoline for the Full Coverage configuration (red line).

The shifted shock presents an increased pressure jump, resulting in a larger contribution to the total pressure drag. As shown in previous studies (Berizzi *et al.*, 2025; Mele & Tognaccini, 2018), this phenomenon explains why skin friction reduction techniques in transonic configurations lead to a lower drag reduction compared to incompressible cases. This behavior is confirmed for the present configuration. Compared to the incompressible cases described within the validation process, the drag reduction is penalized, yielding only $\Delta C_D = -3.1\%$ at $\mathrm{Re}_\infty = 3 \cdot 10^5$ and -0.9% at $\mathrm{Re}_\infty = 10^6$, while the lift enhancement is significantly amplified, reaching $\Delta C_L = +4.2\%$ and $+3.1\%$ at the respective Reynolds numbers.

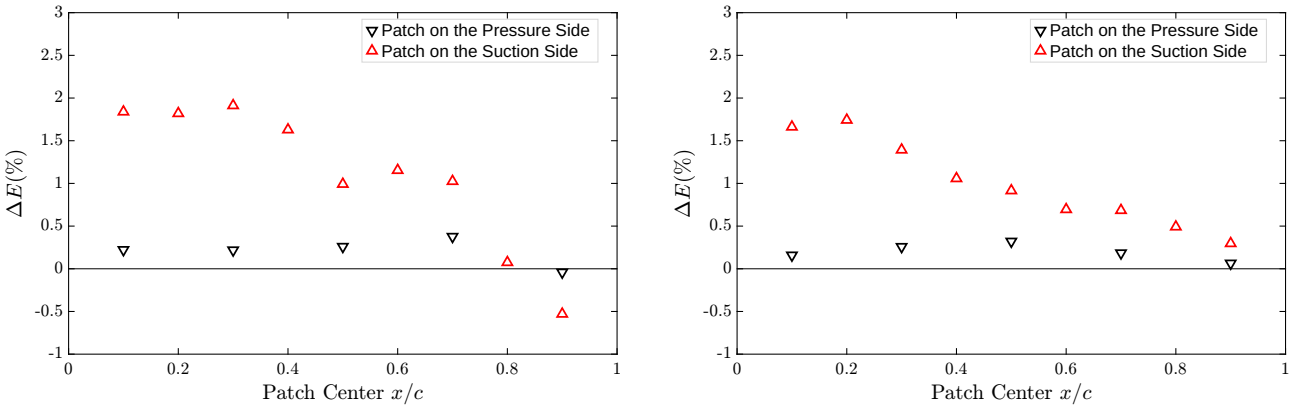

Figure 5: ΔE plotted against the center of the patch at $\mathrm{Re}_\infty = 3 \cdot 10^5$ (left) and $\mathrm{Re}_\infty = 10^6$ (right)

In order to assess the spatial sensitivity of riblet effectiveness, the performance of the localized patches is considered. In Table 2 the outcomes are expressed as percentage variations relative to the Baseline configuration for both efficiency and aerodynamic coefficients. The lift-to-drag ratio variation associated with each patch is plotted in Figure 5. The results describe, under both the considered flow conditions, the suction side as the most sensitive to riblet application. In particular, the highest performance is achieved for riblets positioned upstream of the shock, showing the most evident effect on all the considered parameters. The effectiveness reduces as the

location is moved towards the trailing edge, downstream from the shock wave. The riblet application on the pressure side is still beneficial but causes lower improvements in terms of variations in lift-to-drag ratio. The comparison between the results obtained in the two flow regimes indicates that the presence of riblets alters the flowfield consistently across the two Reynolds numbers. However, as the Reynolds number increases, the effect quantitatively reduces, leading to a lower variation in aerodynamic coefficients.

Table 2: Riblet effectiveness with position as percentage variations of lift-to-drag ratio (ΔE), lift coefficient (ΔC_L) and drag coefficient (ΔC_D). The best performing patch in terms of ΔE is highlighted in bold.

	$\mathrm{Re}_\infty = 3 \cdot 10^5$			$\mathrm{Re}_\infty = 10^6$		
Case ID	ΔE	ΔC_L	ΔC_D	ΔE	ΔC_L	ΔC_D
Baseline	-	-	-	-	-	-
SS0.1	+1.8%	+1.3%	-0.6%	+1.7%	+1.4%	-0.3%
SS0.2	+1.8%	+1.1%	-0.8%	**+1.7%**	**+1.4%**	**-0.4%**
SS0.3	**+1.9%**	**+1.2%**	**-0.7%**	+1.4%	+1.3%	-0.1%
SS0.4	+1.6%	+1.0%	-0.6%	+1.1%	+0.9%	-0.2%
SS0.5	+1.0%	+0.6%	-0.4%	+0.9%	+1.1%	+0.1%
SS0.6	+1.2%	+0.8%	-0.4%	+0.7%	+0.9%	+0.2%
SS0.7	+1.0%	+0.7%	-0.4%	+0.7%	+0.8%	+0.2%
SS0.8	+0.1%	+0.1%	+0.0%	+0.5%	+0.4%	-0.1%
SS0.9	-0.5%	-0.3%	+0.3%	+0.3%	+0.1%	-0.2%
PS0.9	-0.0%	+0.3%	+0.3%	+0.1%	+0.1%	+0.1%
PS0.7	+0.4%	+0.3%	-0.1%	+0.2%	+0.2%	0.0%
PS0.5	+0.3%	+0.2%	-0.1%	+0.3%	+0.2%	-0.1%
PS0.3	+0.2%	+0.2%	-0.1%	+0.3%	+0.1%	-0.2%
PS0.1	+0.2%	+0.2%	-0.1%	+0.2%	+0.1%	-0.1%
Full Coverage	+7.4%	+4.2%	-3.1%	+4.1%	+3.1%	-0.9%

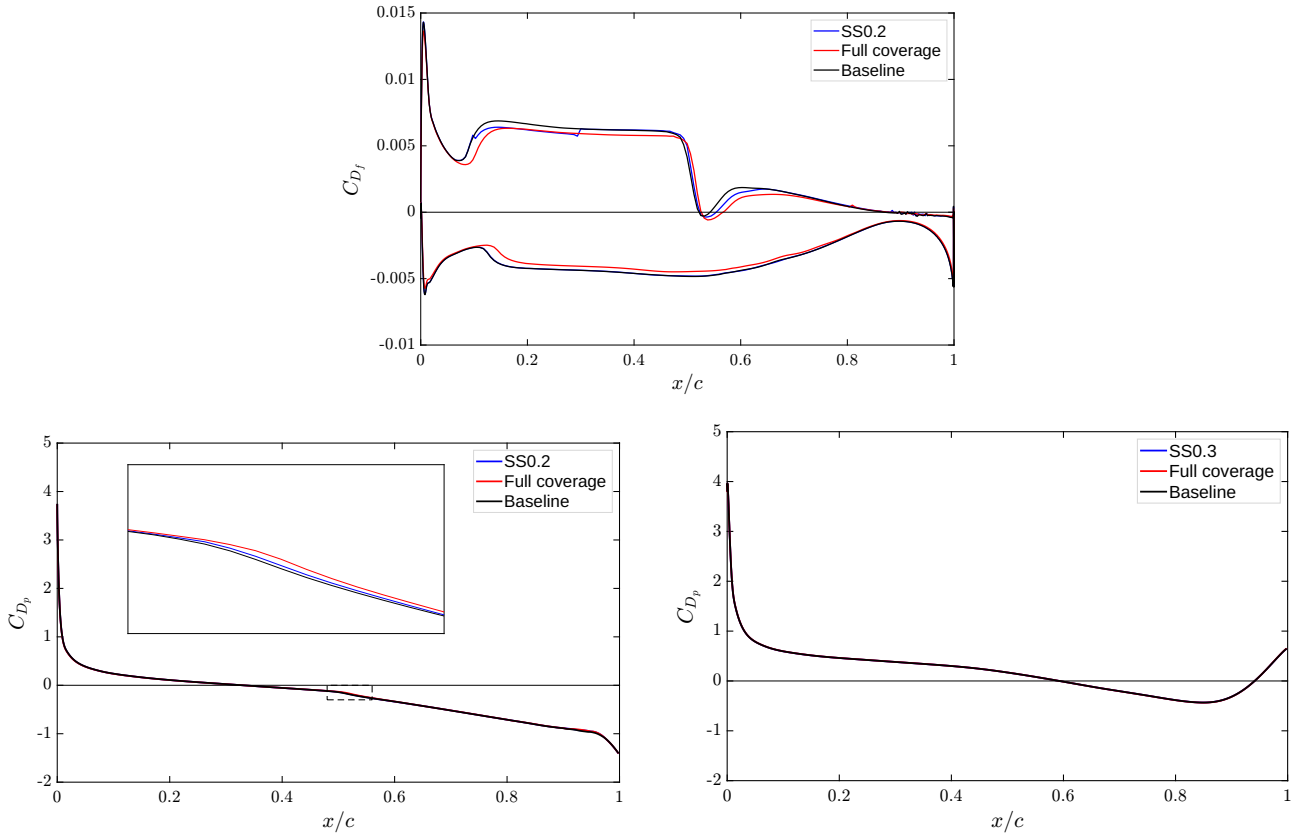

Figure 6: Drag contributions divided by friction (top) and pressure (bottom-left suction side, bottom-right pressure side) for the Baseline, Full Coverage and SS0.2 configurations at $\mathrm{Re}_\infty = 10^6$.

While the shock displacement is the primary cause of the riblet-induced lift variation, the riblet effect on drag is

assessed by analyzing the pressure and the friction contributions separately. These distributions are reported in Figure 6 for the Baseline case, the Full Coverage case and the best-performing patch at $\mathrm{Re}_\infty = 10^6$. As already observed for the friction coefficient, riblets reduce the local skin friction contribution to the drag at each point of application. The C_{D_f} distribution for the best-performing patch highlights how, despite their local effect on skin friction reduction, riblets extend their effectiveness even downstream of the application point. The shift in the shock wave position causes the skin friction drag to evolve differently over a large part of the suction side, even though the patch is applied only over a limited area. Comparing the pressure contribution to the total drag in the three cases, it can be observed that the main differences are localized on the suction side, at the shock location; the shift of the pressure drop is reflected in the shift of the slope change in the C_{D_p} distribution caused by the shock. The Baseline configuration exhibits a lower pressure drag contribution in that region compared to the fully and partially controlled case. This behaviour confirms the concept expressed qualitatively for the Full Coverage configuration: the shock displacement, while beneficial for lift, negatively affects the pressure drag of the airfoil. Importantly, while the relative variations in C_{D_p} appear less pronounced than those in C_{D_f}, the baseline values of these two coefficients differ by two orders of magnitude. As a result, their absolute impact on the total drag is comparable, making the pressure drag increase and the skin friction drag reduction competing effects.

4. Discussion

Since riblets act by altering the physics of the near-wall flow, it is interesting to investigate the performance variations described in the previous section by studying the main quantities representing the characteristics and the state of the boundary layer. The quantities taken into account for both the Reynolds numbers are the displacement thickness δ^* and the momentum thickness θ, defined as follows:

$$\begin{aligned} \delta^* &= \int_0^\delta \left(1 - \frac{\rho u}{\rho_e U_e}\right) dy \\ \theta &= \int_0^\delta \frac{\rho u}{\rho_e U_e}\left(1 - \frac{u}{U_e}\right) dy \end{aligned} \tag{15}$$

where δ is the boundary layer thickness, defined as the wall-normal distance where the velocity magnitude is 99% of the maximum velocity, and the quantities with the subscript 'e' are evaluated at the boundary layer edge. δ^* represents the mass deficit within the boundary layer with respect to the inviscid solution while θ represents the momentum deficit. These quantities are extracted for the Baseline and the Full Coverage configurations. Three points of evaluation are chosen: one at $x/c = 0.38$, upstream of the shock where the boundary layer is already developed; one at $x/c = 0.7$, downstream of the shock but before separation and one at $x/c = 0.99$, representing the trailing edge.

Table 3: Displacement thickness δ^* and momentum thickness θ for the Baseline and Full Coverage cases at the two Reynolds numbers. The subscript '1' indicates a quantity evaluated at $x/c = 0.38$, '2' at $x/c = 0.7$ and '3' at $x/c = 0.99$

		δ_1^*	δ_2^*	δ_3^*	θ_1	θ_2
$Re_\infty = 3 \cdot 10^5$	Baseline	0.001986	0.007151	0.043120	0.000769	0.002844
	Full Coverage	0.001858	0.007122	0.042144	0.000709	0.002828
$Re_\infty = 10^6$	Baseline	0.001589	0.006926	0.040922	0.000722	0.002809
	Full Coverage	0.001471	0.007149	0.039922	0.000669	0.002808

Table 3 reports the values of the displacement and momentum thickness for the Baseline and Full Coverage configurations at both Reynolds numbers. The riblet application alters the boundary layer characteristics around the airfoil. Upstream of the shock, the control induces a reduction in both mass and momentum deficits at both Reynolds numbers. This modification in the boundary layer allows the flow to accelerate more effectively, consistent with the enlarged supersonic region observed earlier. At $x/c = 0.7$ it is possible to notice the effect of a delayed shock: the increased intensity and delayed position steepen the adverse pressure gradient within the boundary layer, leading to an increase in the displacement thickness. The net effect of an increased post-shock pressure gradient acting on a thinner incoming boundary layer is a marginal reduction in δ^* for the low-Reynolds-number case, and a slight increase for the high-Reynolds-number case. δ^* is also extracted at the trailing edge as a measurement of the negative effect of the separation bubble that characterizes the considered

case. Riblets mitigate adverse flow features by decreasing the size of the separated region; this reduces the effective thickening of the airfoil, lowering the pressure contribution to the drag and enhancing performance.
It is also interesting to compare the boundary layer state between the Baseline cases at both Reynolds numbers. The high Reynolds number case clearly features a thinner boundary layer in all the considered points, with a reduced separation bubble. At high Re, the boundary layer dissipates less mass and momentum and the shock position is moved downstream; this limits the potential to improve the boundary layer characteristics and to increase lift through the shock shift towards the trailing edge.

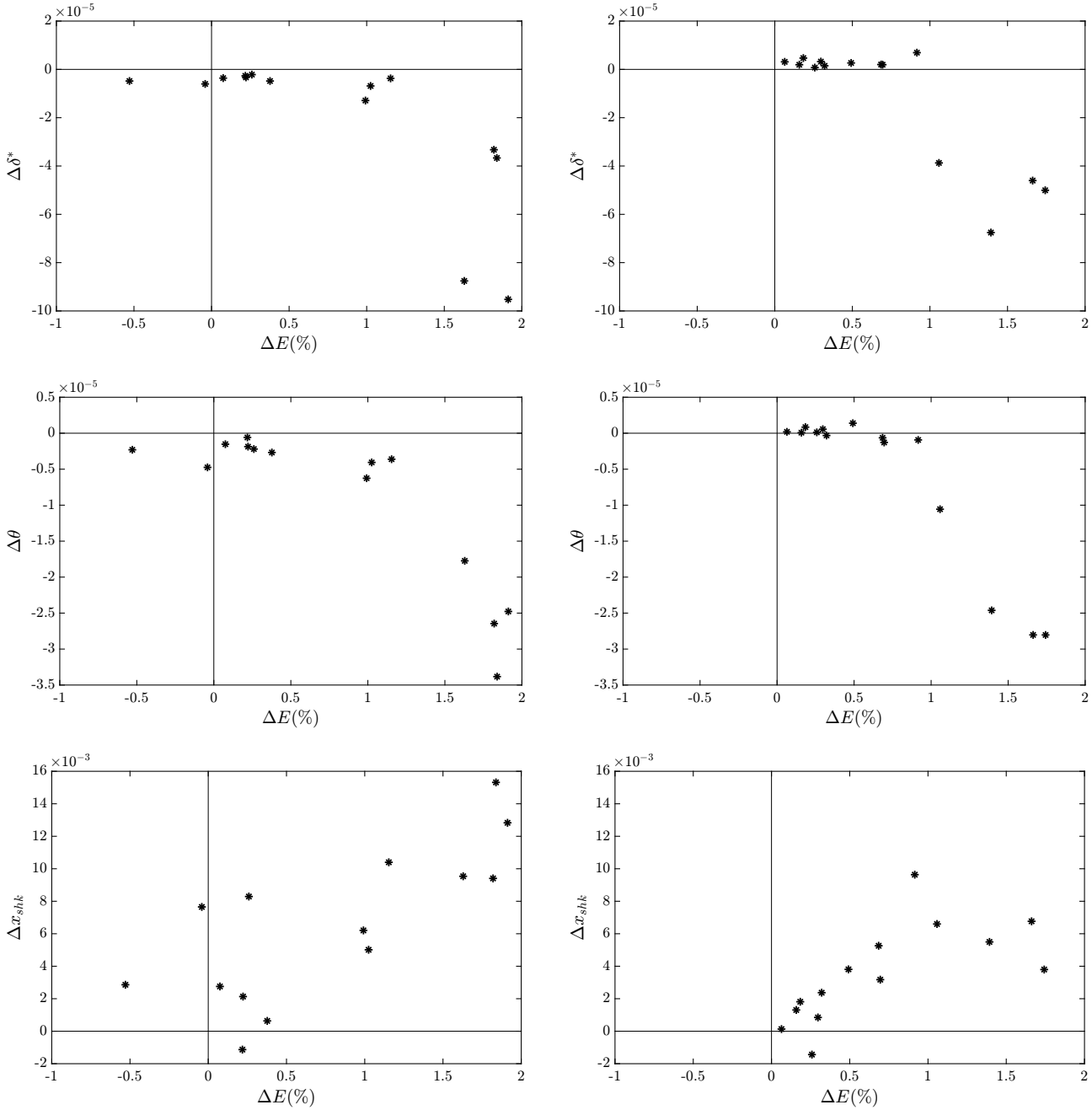

Figure 7: Relation between upstream boundary layer variations ($x/c = 0.38$) and shock displacement against efficiency. Left panels represent quantities evaluated at $\mathrm{Re}_\infty = 3 \cdot 10^5$ while the right panels correspond to $\mathrm{Re}_\infty = 10^6$

The results reported up to now show that the application of a skin friction reduction device such as riblets interacts with the physics of a transonic profile not only by acting on the skin friction coefficient at the point of application. Specifically, such devices alter the boundary layer, shift the shock position and affect the separated region. In order to understand the root causes that govern the drag reduction in this case, the relation between these characteristics and the variation in performance is investigated for the partial coverage configurations. To highlight the relationship between local flow modifications and global performance, Figure 7 displays the

changes in the boundary layer thickness extracted at $x/c = 0.38$ ($\Delta\delta^*, \Delta\theta$) and shock position ($\Delta x_{shk}$) as a function of the variation in aerodynamic efficiency (ΔE). All quantities represent the deviation of each patch from the Baseline case. Each variational quantity referred to the simulation i is defined as follows:

$$\Delta X_i = X_i - X_{baseline} \tag{16}$$

Although a strict correlation between these quantities across the Reynolds numbers is not found, it is shown that the largest variations of the considered flow features correspond to the greatest performance enhancements and a qualitative trend emerges for certain quantities. At $\mathrm{Re}_\infty = 3 \cdot 10^5$ the application of riblets causes higher variations of the boundary layer variables and shock position with respect to $\mathrm{Re}_\infty = 10^6$. A consistent behaviour links $\Delta\theta$, Δx_{shk} and the variation in performance, while $\Delta\delta^*$ is less related to ΔE. The only patches that significantly reduce δ^* and θ upstream of the shock are those located at or in proximity to the evaluation point. Hence, they naturally influence the local boundary layer more than the other patches, without this necessarily implying that minimizing the boundary layer at this location directly causes the performance improvement. The lack of a clear correlation between the lift-to-drag ratio and a single parameter highlights an important feature of skin friction reduction applied to transonic airfoils. The variations induced by riblet application alter the flowfield in a complex way, producing competing effects. On one hand, the application of riblets acts locally, reducing the mass and momentum deficit within the boundary layer. This localized improvement modifies the flow development and displaces the shock wave, enhancing performance. On the other hand, the shock shift increases the shock contribution to pressure drag and the adverse pressure gradient downstream, making the boundary layer more prone to separation. An enlarged separated region negatively affects the airfoil performance by further increasing the pressure drag.

5. Adjoint formulation

The numerical solver developed in this work represents only the first building block of a complete design tool. While a parametric study like the current one highlights the location where the application of riblets is most effective, it fails to provide the absolute best configuration and quickly becomes computationally inefficient when a three-dimensional case is considered. Furthermore, such an approach relies on an arbitrary patch length, whereas the spatial extent of the riblet treatment should be part of the optimization process. The definitive numerical framework is obtained by integrating the developed flow solver with an adjoint solver performing the optimization. This combination creates a fully automated numerical tool, capable of optimizing both the placement and the surface extent of the riblets. The final objective is to minimize an economic cost function that balances the fuel savings derived from aerodynamic improvements against the operational and maintenance costs associated with the total area of the ribbed surface. To lay the groundwork for this integration, the derivation of the compressible adjoint equations and their corresponding boundary conditions is presented below, establishing the theoretical framework to compute the sensitivity of aerodynamic loads to the partial slip formulation.

One of the most widely used methods for numerical optimization is the implementation of gradient-based algorithms (Martins & Hwang, 2013). These algorithms exploit the sensitivity of the solution with respect to the control variables, iteratively updating the latter to achieve the minimum or the maximum value of a target quantity. The most computationally challenging task in this process is the computation of the sensitivity, namely the gradient of the objective function with respect to the control parameters, especially when a large number of parameters are involved. Solving the adjoint equations is one of the most efficient ways to compute the sensitivity in complex configurations, since the computational cost is independent of the number of design variables. Therefore, deriving these equations and computing the expressions of lift and drag sensitivity to the application of a tangential slip at the wall are fundamental steps towards the spatial optimization of skin-friction reduction devices.

In Appendix B the derivation of the adjoint equations and the corresponding boundary conditions is summarized. Starting from the original simulation, it is possible to compute the values of the adjoint variables ζ, $\boldsymbol{\chi}$ and η by solving the equations reported in Eq.(17) while enforcing the boundary conditions summarized in Table 4.

$$\begin{aligned}
&-\rho\nabla\zeta - \rho\boldsymbol{u}\cdot\nabla\boldsymbol{\chi} - \rho(\nabla\boldsymbol{\chi})^T\boldsymbol{u} + \eta\rho C_p\nabla T - \eta\nabla p + \nabla\cdot(\eta\boldsymbol{\tau}) - \mu(\nabla\cdot\boldsymbol{\tau}^*) = 0 \\
&-\nabla\cdot\boldsymbol{\chi} + \nabla\cdot(\eta\boldsymbol{u}) + \left(\frac{1}{RT}\right)[-\boldsymbol{u}\cdot\nabla\zeta + \boldsymbol{\chi}\cdot(\boldsymbol{u}\cdot\nabla\boldsymbol{u}) + \eta C_p(\boldsymbol{u}\cdot\nabla T)] = 0 \\
&C_p\rho\boldsymbol{u}\cdot\nabla\eta + \nabla\cdot(k\nabla\eta) + \left(\frac{\rho}{T}\right)[-\boldsymbol{u}\cdot\nabla\zeta + \boldsymbol{\chi}\cdot(\boldsymbol{u}\cdot\nabla\boldsymbol{u}) + \eta C_p(\boldsymbol{u}\cdot\nabla T)] = 0
\end{aligned} \tag{17}$$

Once the adjoint variables are obtained in the domain it is possible to compute the sensitivity of the target quantities to the application of a slip length λ at the wall. The sensitivity of the drag ($\nabla_\lambda D$) results in:

$$\nabla_\lambda D = \left(\frac{\partial\boldsymbol{u}}{\partial\boldsymbol{n}}\right)_w [\zeta\rho\boldsymbol{n} + \rho(\boldsymbol{u}\cdot\boldsymbol{\chi})\cdot\boldsymbol{n} - \eta\boldsymbol{\tau}\cdot\boldsymbol{n} + \mu\boldsymbol{\tau}^*\cdot\boldsymbol{n}] \tag{18}$$

Table 4: Adjoint boundary conditions for transonic RANS corresponding to the numerical setup defined in Table 6

Inlet	Outlet	Airfoil Surface
$\frac{\partial \zeta}{\partial \boldsymbol{n}} = 0$	$\zeta \rho \boldsymbol{n} + (\rho \boldsymbol{u} \cdot \boldsymbol{n}) \boldsymbol{\chi} + \rho (\boldsymbol{u} \cdot \boldsymbol{\chi}) \cdot \boldsymbol{n} - \eta \boldsymbol{\tau} \cdot \boldsymbol{n} + \mu \boldsymbol{\tau}^* \cdot \boldsymbol{n} = 0$	$\boldsymbol{\chi} = \hat{\boldsymbol{i}}$
$\boldsymbol{\chi} = 0$	$\left(\frac{1}{RT}\right) \zeta \boldsymbol{u} \cdot \boldsymbol{n} + \boldsymbol{\chi} \cdot \boldsymbol{n} - \eta (\boldsymbol{u} \cdot \boldsymbol{n}) = 0$	$\frac{\partial \zeta}{\partial \boldsymbol{n}} = 0$
$\eta = 0$	$\eta \rho C_p \boldsymbol{u} \cdot \boldsymbol{n} + k (\nabla \eta \cdot \boldsymbol{n}) - \left(\frac{\rho}{T}\right) \zeta \boldsymbol{u} \cdot \boldsymbol{n} = 0$	$\frac{\partial \eta}{\partial \boldsymbol{n}} = 0$

Similarly, the derivation for lift ($\nabla_\lambda L$) yields the exact same algebraic expression:

$$\nabla_\lambda L = \left(\frac{\partial \boldsymbol{u}}{\partial \boldsymbol{n}} \right)_w [\zeta \rho \boldsymbol{n} + \rho (\boldsymbol{u} \cdot \boldsymbol{\chi}) \cdot \boldsymbol{n} - \eta \boldsymbol{\tau} \cdot \boldsymbol{n} + \mu \boldsymbol{\tau}^* \cdot \boldsymbol{n}] \tag{19}$$

with the only difference being that the boundary condition for the adjoint velocity at the airfoil switches from $\boldsymbol{\chi} = \hat{\boldsymbol{i}}$ to $\boldsymbol{\chi} = \hat{\boldsymbol{j}}$. This changes the values of the adjoint variables in the domain, hence the sensitivity value.
As already described in Section 3, it is interesting to compute the sensitivity of the lift-to-drag ratio E to the application of a slip length λ ($\nabla_\lambda E$), rather than the sensitivity of lift and drag separately. To achieve this, the method proposed by Ohashi *et al.* (2021) is presented, computing $\nabla_\lambda E$ from the values of $\nabla_\lambda L$ and $\nabla_\lambda D$ using the quotient rule for differentiation:

$$\nabla_\lambda E = \nabla_\lambda (L/D) = \frac{D_0 \nabla_\lambda L - L_0 \nabla_\lambda D}{D_0^2} \tag{20}$$

where L_0 and D_0 are the lift and the drag forces in the original simulation.

6. Conclusions

The purpose of this work was to investigate the spatial sensitivity of aerodynamic performance to riblet placement in compressible transonic flows. To evaluate the impact of the application point on the lift-to-drag ratio of the airfoil, a series of RANS simulations, each featuring a different riblet location, was performed. A partial slip boundary condition for velocity models the effect of locally optimal riblets, consistent with both theoretical and experimental studies available in the literature.
Initially, the implemented setup was validated in widely studied incompressible cases, reproducing available results for a flat plate and a NACA 0012 at varying incidence. After the validation, it was applied to model riblet effect in a more complex transonic case at two different Reynolds numbers.
The riblet application in the transonic scenario causes, in addition to the skin friction reduction which is the primary effect, a redistribution of the pressure that induces a shift of the shock wave towards the trailing edge. This enhances lift significantly while also contributing to an increase in the pressure drag. The global effect on the lift-to-drag ratio is governed by a trade-off between friction drag reduction and shock-induced pressure drag penalties, but was assessed to be positive in almost every tested configuration. When the airfoil is entirely covered by riblets, the global flow alteration is substantial enough to compensate for the negative effects associated with the increased shock intensity. In contrast, partial coverage configurations introduce reduced flow modifications, making the variation in efficiency dependent on the trade-off between positive and adverse effects. Notably, applying riblets to the forward section of the suction side, upstream of the shock wave, yields the most significant changes in flow features producing the highest benefit on the airfoil performance. Altering the boundary layer over this initial region has the greatest effect on the flow developing over the aerodynamically critical sections of the airfoil, resulting in greater performance improvements. The results of the study, performed at two different Reynolds numbers, exhibit the same trend while presenting quantitative differences: as the Reynolds number increases, riblet application is characterized by a reduced influence on both shock displacement and lift-to-drag ratio.
While a parametric study like the one presented here can be insightful, it is limited in resolution by its discrete nature and it is computationally prohibitive for three-dimensional applications. Further studies can improve this analysis by employing an optimization algorithm. A highly promising approach is to apply an adjoint-based optimization to extend it to the three-dimensional case in an efficient way. In order to do so, the adjoint equations for compressible RANS, using as control parameters the slip length at the wall, and the corresponding boundary conditions were derived. The implementation of a solver capable of performing this adjoint simulation is the first step towards a rigorous and computationally efficient optimization of skin friction reduction placement on aerodynamic surfaces.

References

Aupoix, B., Pailhas, G. & Houdeville, R. 2012 Towards a General Strategy to Model Riblet Effects. *AIAA Journal* **50** (3), 708–716.

Bechert, D.W. & Bartenwerfer, M. 1989 The viscous flow on surfaces with longitudinal ribs. *J. Fluid Mech.* **206**, 105–209.

Bechert, D.W., Bruse, M., Hage, W., Hoeven, J.G.T. Van Der & Hoppe, G. 1997 Experiments on drag-reducing surfaces and their optimization with an adjustable geometry. *J. Fluid Mech.* **338**, 59–87.

Berizzi, N., Gatti, D., Soldati, G., Pirozzoli, S. & Quadrio, M. 2025 Aerodynamic performance of a transonic airfoil with spanwise forcing. *J. Fluid Mech.* **1010**, A18.

Cacciatori, L., Brignoli, C., Mele, B., Gattere, F., Monti, C.M. & Quadrio, M. 2022 Drag Reduction by Riblets on a Commercial UAV. *Appl. Sci.* **12** (10), 5070.

Debisschop, J. & Nieuwstadt, F. 1996 Turbulent Boundary Layer in an Adverse Pressure Gradient: Effectiveness of Riblets. *AIAA Journal* **34** (5), 932–937.

Doerffer, P., Flaszynski, P., Dussauge, J.-P., Babinsky, H., Grothe, P., Petersen, A. & Billard, F., ed. 2021 *Transition Location Effect on Shock Wave Boundary Layer Interaction: Experimental and Numerical Findings from the TFAST Project*, *Notes on Numerical Fluid Mechanics and Multidisciplinary Design*, vol. 144. Springer International Publishing.

Gad-el-Hak, M. 2000 *Flow Control – Passive, Active and Reactive Flow Management*. Cambridge University Press, Cambridge.

García-Mayoral, R. & Jiménez, J. 2011 Drag reduction by riblets. *Phil. Trans. R.Soc. A* **369** (1940), 1412–1427.

Garcia-Mayoral, R. & Jiménez, J. 2011 Hydrodynamic stability and the breakdown of the viscous regime over riblets. *Journal of Fluid Mechanics* **678**, 317–347.

Gómez-de-Segura, G., Fairhall, C. T., MacDonald, M., Chung, D. & García-Mayoral, R. 2018 Manipulation of near-wall turbulence by surface slip and permeability. *J. Phys.: Conf. Ser.* **1001** (1), 012011.

Graver, B., Zhang, K. & Rutherford, D. 2019 CO2 emissions from commercial aviation, 2018. *Tech. Rep.*. International Council on Clean Transportion.

Klöwer, Milan, Allen, Myles, Lee, David, Proud, Simon, Gallagher, Leo & Skowron, Agnieszka 2021 Quantifying aviation's contribution to global warming.

Koepplin, V., Herbst, F. & Seume, J. R. 2017 Correlation-based riblet model for tubomachinery applications. *Journal of Turbomachinery* **139**.

Luchini, P. 1996 Reducing the turbulent skin friction. In *Computational Methods in Applied Sciences 1996* (ed. Desideri et al.), pp. –. Wiley.

Luchini, P. 2017 Universality of the Turbulent Velocity Profile. *Phys. Rev. Lett.* **118** (22), 224501.

Luchini, P., Manzo, F. & Pozzi, A. 1991 Resistance of a grooved surface to parallel flow and cross-flow. *J. Fluid Mech.* **228**, 87–109.

Martins, Joaquim & Hwang, John 2013 Review and Unification of Methods for Computing Derivatives of Multidisciplinary Computational Models. *AIAA Journal* **51**, 2582–2599.

Maxwell, J. Clerk 1879 On Stresses in Rarified Gases rising from Inequalities of Temperature. *Philosophical Transactions of the royal Society of London* **170**, 231–256.

Mele, B. & Tognaccini, R. 2012 Numerical Simulation of Riblets on Airfoils and Wings. In *50th AIAA Aerospace Sciences Meeting Including the New Horizons Forum and Aerospace Exposition*. American Institute of Aeronautics and Astronautics.

Mele, B. & Tognaccini, R. 2018 Slip Length–Based Boundary Condition for Modeling Drag Reduction Devices. *AIAA Journal* **56** (9), 3478–3490.

Mele, B., Tognaccini, R. & Catalano, P. 2016 Performance assessment of a transonic wing-body configuration with riblets installed. *J. Aircr.* **53** (1), 129–140.

Menter, F.R. 1994 Two-Equation Eddy-Viscosity Turbulence Models for Engineering Applications. *AIAA J.* **32** (8), 1598–1605.

Navier, M. 1823 "Mémoire sur le lois du mouvement des fluides,". *Mémoire del'Académie Royale des ciences de l'Institut de France VI* **6**, 389–440.

Ohashi, M., Fukagata, K. & Tokugawa, N. 2021 Adjoint-Based Sensitivity Analysis for Airfoil Flow Control Aiming at Lift-to-Drag Ratio Improvement. *AIAA Journal* **59** (11), 4437–4448.

Quadrio, M., Chiarini, A., Banchetti, J., Gatti, D., Memmolo, A. & Pirozzoli, S. 2022 Drag reduction on a transonic airfoil. *J. Fluid. Mech.* **942**, R2, 1–10.

Quadrio, M., Ricco, P. & Viotti, C. 2009 Streamwise-traveling waves of spanwise wall velocity for turbulent drag reduction. *J. Fluid Mech.* **627**, 161–178.

Schramm, M., Stoevesandt, B. & Peinke, J. 2018 Optimization of Airfoils Using the Adjoint Approach and the Influence of Adjoint Turbulent Viscosity. *Computation* **6** (1), 5.

Sundaram, S., Viswanath, P.R. & Rundrakumar, S. 1996 Viscous drag reduction using riblets on NACA 0012 airfoil to moderate incidence. *AIAA Journal* **34** (4).

Szodruch, J. 1991 Viscous drag reduction on transport aircraft. In *29th Aerospace Sciences Meeting*. Reno,NV (U.S.A.): American Institute of Aeronautics and Astronautics.

Viswanath, P.R. 2002 Aircraft viscous drag reduction using riblets. *Progress in Aerospace Sciences* **38**, 571–600.

Walsh, M.J. 1980 Drag characteristics of v-groove and transverse curvature riblets. *In Viscous Drag reduction (ed. G.R. Hough). American Institute of Aeronautics and Astronautics.* .

Walsh, M. J. & Weinstein, L. M. 1979 Drag and Heat-Transfer Characteristics of Small Longitudinally Ribbed Surfaces. *AIAA Journal* **17** (7), 770–771.

Weller, H.G., Tabor, G., Jasak, H. & Fureby, C. 1998 A tensorial approach to computational continuum mechanics using object-oriented techniques. *Computers in Physics* **12** (6), 620–631.

Wilcox, D.C. 2006 *Turbulence Modeling for CFD*, , vol. 3. DCW industries La Cañada, CA.

A. Computational Setup and Validation

The reliability of the numerical results obtained in this study inherently depends on the accuracy of the underlying computational setup. For this reason, before investigating the riblet effect in a transonic configuration, it is mandatory to build a reliable numerical environment. To achieve this goal, both the boundary condition effectiveness and the transonic setup are validated. The capability of the numerical environment to impose a prescribed upward shift on the velocity profile is tested in standard incompressible cases, already described by Mele & Tognaccini (2012) and Cacciatori *et al.* (2022). These are a flat plate and a NACA 0012 profile at incidence 0° and 4°, which allows the assessment of the effectiveness of the implemented boundary condition in the presence of a pressure gradient. The Baseline case of the V2C profile in transonic conditions is validated against the results obtained through DNS by Berizzi *et al.* (2025).

A.1. Incompressible Cases

The incompressible simulations are carried out under steady-state conditions using the *incompressibleFluid* module solver in OpenFOAM, able to represent incompressible, isothermal turbulent flow in both steady and unsteady regimes. The SIMPLE (Semi-Implicit Method for Pressure Linked Equations) algorithm is used to solve the RANS equations, all spatial differential operators are numerically approximated using a second-order discretization.
The first considered case is a flat plate at freestream Reynolds number $\mathrm{Re}_\infty = \frac{U_\infty L}{\nu} = 10^6$ where $L = 2m$ is the plate length. The turbulence is modelled using the $k-\omega$ SST model (Menter, 1994) with a freestream turbulent-to-laminar viscosity ratio of 0.001 and a freestream turbulence intensity $TU_\infty = 0.5\%$. The computational

domain is rectangular with length 2.3 m and height 1 m, where a symmetry boundary condition is enforced in the first 0.3 m in order to make the flow develop before approaching the flat plate. It features a structured mesh, generated with the *blockMesh* utility, composed of 500 hexahedral cells in the freestream direction and 250 cells in the wall-normal direction. Cells are clustered at the leading edge of the flat plate to correctly represent the boundary layer development and the wall-normal cell dimension presents a geometric progression in order to obtain $y^+ < 1$ at the wall keeping the number of the cells manageable.

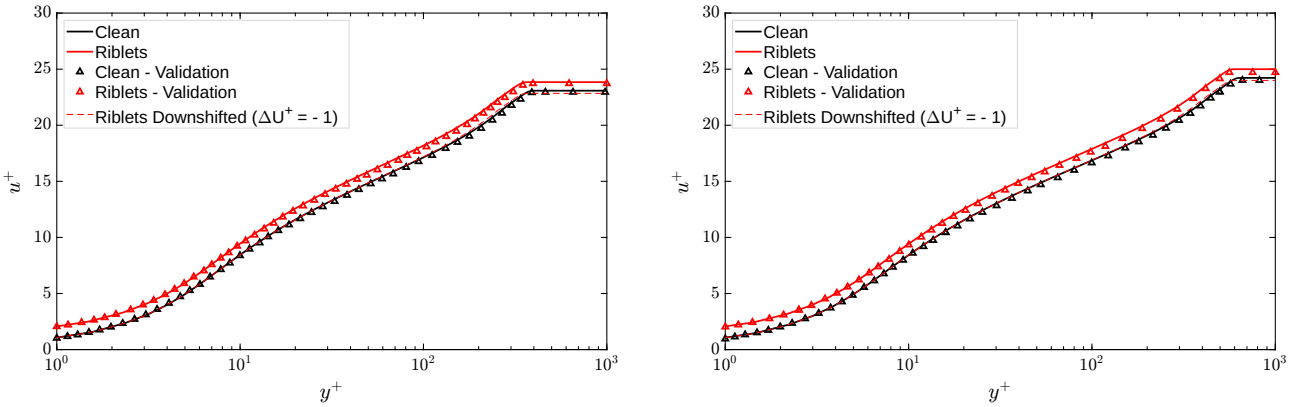

Figure 8: Velocity profile extracted at $\mathrm{Re}_x = 5 \cdot 10^5$ (left) and $\mathrm{Re}_x = 9 \cdot 10^5$ (right) compared with the results obtained by Cacciatori *et al.* (2022).

The results obtained by applying the slip length boundary condition on the entire flat plate, imposing $\lambda^+ = \Delta U^+ = 1$, are compared with a standard no-slip flat plate. The velocity profiles are extracted at two different points of the flat plate, where the turbulent regime is already established (in this case for $\mathrm{Re}_x > 10^5$). It is shown in Figure 8 that the implemented boundary condition is able to impose a prescribed upward shift of the velocity profile at different locations on the flat plate that feature different flow conditions. The downshift of the velocity profile extracted from the ribbed flat plate overlaps correctly with the one extracted from the clean flat plate, proving that the shift is correctly imposed on the entire velocity profile, rather than solely at the wall.
The friction coefficient evolution along the flat plate is presented in Figure 9. Once the turbulent regime is established, the present boundary condition is able to correctly represent the skin friction drag reduction in agreement with previous works.

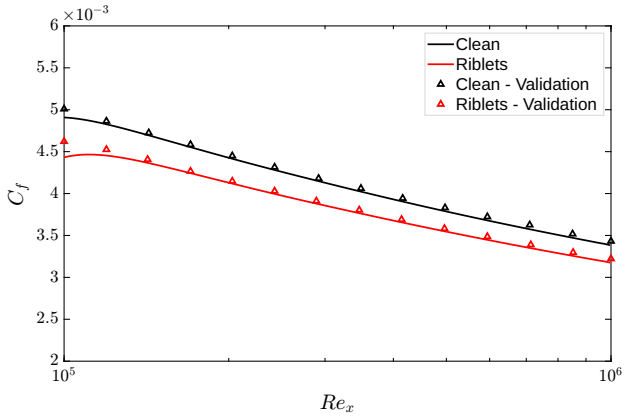

Figure 9: Evolution of the friction coefficient along the flat plate in turbulent regime. compared with the results obtained by Cacciatori *et al.* (2022).

The validation process is extended to the riblet application on a NACA 0012 airfoil at incidence α of 0° and 4°. The airfoil is tested considering a freestream Reynolds number $\mathrm{Re}_\infty = 10^6$ using the unit chord c as reference length. RANS equations are solved coupled with the $k-\omega$ SST turbulence model imposing a freestream turbulent-to-laminar viscosity ratio of 0.001 and a freestream turbulence intensity $TU_\infty = 5\%$. In order to perform the simulations, a structured C-Grid is generated; it extends in every direction for a length of $30c$ and it is formed by 630 cells around the airfoil, 130 cells in the freestream direction and 160 in the wall-normal direction. Geometric progression in the freestream direction is used to increase cell density at the leading edge and the trailing edge to model effectively boundary layer development and wake evolution, while in the wall-normal direction, the same approach is employed to ensure a maximum $y^+ < 1$ along the entire airfoil.

The same analysis already performed for the flat plate on the velocity profile is reported for the NACA 0012 in Figure 10 which highlights how, in a more complex case, the proposed numerical environment allows a reliable representation of the riblet effect, imposing a prescribed shift of the velocity profile also in the presence of a pressure gradient of variable intensity.

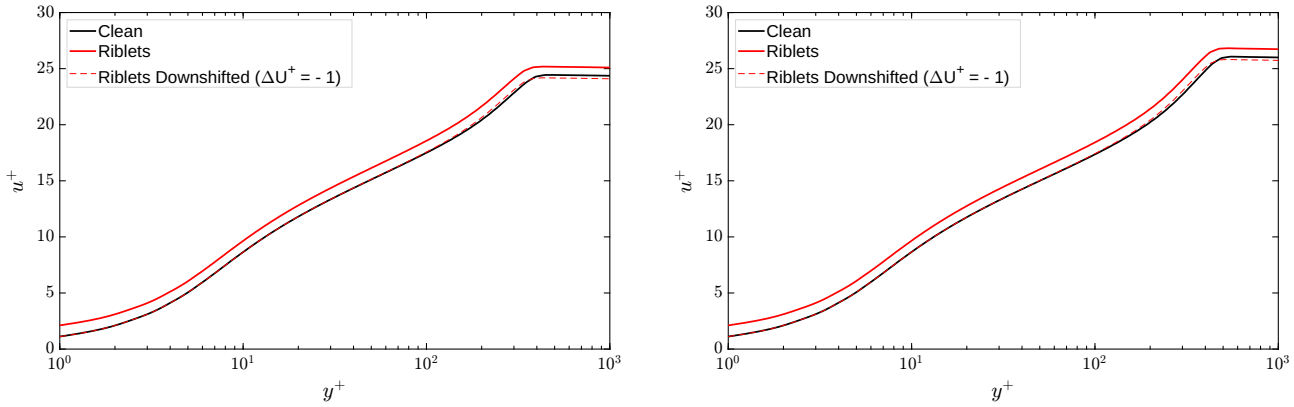

Figure 10: Velocity profile on the NACA 0012 airfoil extracted at $x/c = 0.5$ for $\alpha = 0°$ (left) and $\alpha = 4°$ (right).

The combination of mesh and freestream conditions just described ensures an accurate reproduction of the data produced by Mele & Tognaccini (2012) and Cacciatori *et al.* (2022). As shown in Figure 11, the application of optimal riblets consistently reduces the skin friction even in the presence of a pressure gradient, confirming the correct functioning of the boundary condition implemented in this work and its capability in reproducing reliable data, with the exception of the separation location. Furthermore, the variation of global quantities is in accordance with the cited studies, reporting for $\alpha = 4°$ a $\Delta C_D = -6.4\%$ caused by a 7.3% reduction in the pressure contribution and a 6.4% reduction in the friction contribution. It is interesting to confirm once more the effectiveness of riblets not only on the skin friction, but also on the pressure distribution.
The results presented up to now do not add new information to the findings contained in the studies already performed and considered benchmark for validation, but they ensure the reliability of the newly implemented boundary condition in the representation of the riblet effect in RANS. This framework will be exploited and considered reliable to be applied in cases where direct validation is not available.

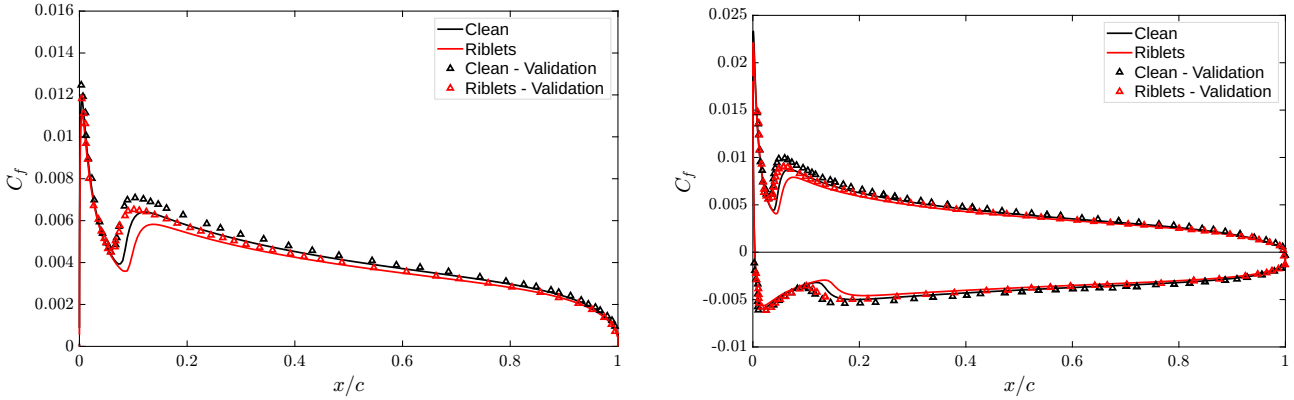

Figure 11: Friction coefficient distribution on NACA 0012 for $\alpha = 0°$ (left) and $\alpha = 4°$ (right) validated against the results obtained by Mele & Tognaccini (2012).

A.2. Compressible Case

Once the boundary condition implementation is verified in incompressible standard cases, it is necessary to verify the compressible numerical environment in which it will be applied. The selected case of interest is the configuration investigated by Berizzi *et al.* (2025): a V2C supercritical airfoil at incidence $\alpha = 4°$, freestream Mach number $\mathrm{Ma}_\infty = 0.7$ and freestream Reynolds number $\mathrm{Re}_\infty = 3 \cdot 10^5$. The compressible RANS equations are solved in steady-state conditions using the pressure-based *fluid* solver implemented in OpenFOAM. Mass conservation is enforced by solving a pressure equation and density is directly computed through the equation

of state. The PIMPLE algorithm is employed to manage the high pressure and density gradients that characterize the representation of a shock. It features an external SIMPLE loop that solves momentum and energy conservation in steady state but contains an inner PISO (Pressure Implicit with Splitting of Operators) loop, solving and correcting the pressure equation multiple times per iteration. Local Time Stepping is used to increase convergence speed of the simulation and differential operators are discretized with second-order schemes. The presence of a shock wave imposes the choice of Total Variation Diminishing (TVD) schemes, which are less prone to non-physical oscillations induced by its numerical approximation. Turbulence effects are modelled with the $k-\omega$ SST model, setting the freestream turbulent-to-laminar viscosity ratio to 0.001 and the freestream turbulence intensity to $TU_\infty = 0.05\%$.
All the simulations are performed using a structured C-Grid. In order to produce a reliable environment, several configurations were tested by studying the sensitivity of the solution to both the farfield location and the mesh density. The chosen mesh, which guarantees the best trade-off between accuracy and computational cost, extends in each direction for a length of $30c$ and presents 550 hexahedral cells around the airfoil, 170 cells in the wake and 185 cells in the wall-normal direction. Mesh stretching already described in previous cases is utilized to strictly assure $y^+ < 1$ and to correctly capture boundary layer and wake development.

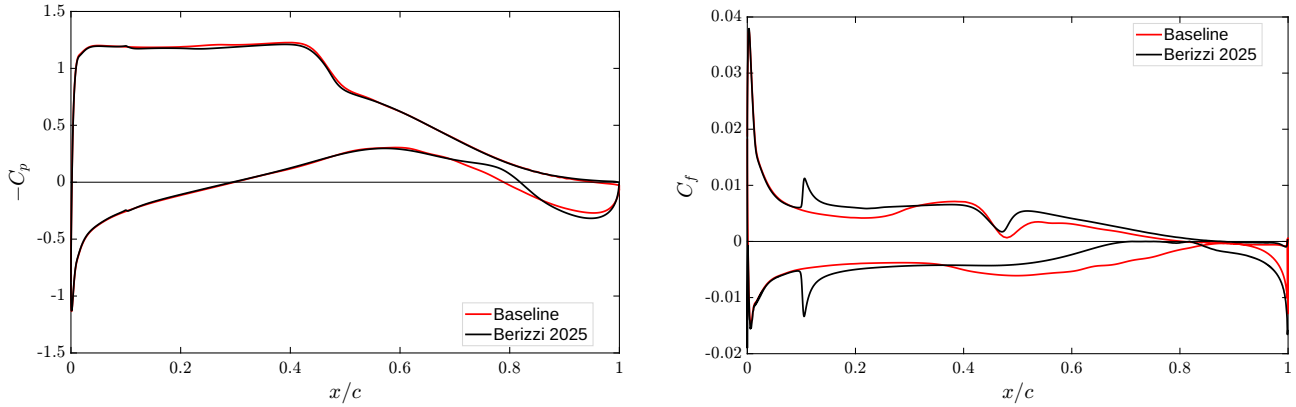

Figure 12: Pressure distribution (left) and friction distribution (right) of the baseline case, compared with the validation DNS.

In Figure 12 the pressure and friction coefficient distributions over the airfoil are reported and compared with those used for validation, obtained through DNS. It is possible to notice that, for large parts of the airfoil, the present numerical setup is able to correctly reproduce the pressure distribution that characterizes the V2C airfoil in the analyzed conditions. The friction coefficient, instead, presents major discrepancies with respect to the baseline case. The major cause identified for this difference, other than the intrinsic accuracy mismatch between DNS and RANS, is the presence of boundary layer tripping in the original simulation, which is not modelled in the current numerical setup; this causes the boundary layer, hence the friction coefficient, to evolve differently between the two cases.
Following the pressure and friction distributions, the global aerodynamic quantities are compared and the results are reported in Table 5. The agreement between the pressure fields results in an accurate estimation of the C_L in the present simulation. However, the discrepancies in the boundary layer development, due to the absence of tripping, cause the RANS simulation to overpredict the flow separation on the suction side (indicated by the negative C_f values) while failing to capture the separation on the pressure side. This affects the computation of the total drag, leading to a significant underprediction of the C_D with respect to the baseline case.

Table 5: C_L and C_D discrepancies between the baseline case and the validation data obtained by Berizzi *et al.* (2025).

	Baseline	Berizzi 2025
C_L	0.759	0.747
C_D	0.0220	0.0242

B. Derivation of the Continuous Adjoint Equations

This appendix contains the mathematical derivation of the continuous adjoint equations, the corresponding boundary conditions, and the sensitivity formulations presented in Section 5.

B.1. Theoretical definition

Any optimization study relies on the identification of the main quantity of interest, which is the object of the process, and its relations with the design and the state variables. The quantity of interest is defined as the objective function $\mathcal{J}(\boldsymbol{x}, \boldsymbol{u})$, where $\boldsymbol{x}$ are the design variables and $\boldsymbol{u}$ are the state variables. State variables are determined by the design variables through the governing equations of the system $\mathrm{R}(\boldsymbol{x}, \boldsymbol{u}) = 0$, which in the present case are the compressible RANS equations described in Section 2. The sensitivity is defined as the gradient of the solution with respect to the design variables; since the state variables depend on the design variables, the gradient can be expressed as:

$$\frac{d\mathcal{J}}{d\boldsymbol{x}} = \frac{\partial \mathcal{J}}{\partial \boldsymbol{x}} + \frac{\partial \mathcal{J}}{\partial \boldsymbol{u}} \frac{d\boldsymbol{u}}{d\boldsymbol{x}} \tag{21}$$

The direct evaluation of the term $\frac{d\boldsymbol{u}}{d\boldsymbol{x}}$ requires performing a numerical simulation for each control parameter, a requirement that quickly makes the computational cost unfeasible as the number of variables increases. In contrast, the formulation of the adjoint equations allows the computation of the sensitivity of the target quantity in the whole domain by performing a single simulation, regardless of the number of control parameters.
In order to define the adjoint equations, it is possible to write the Lagrangian:

$$\mathcal{L}(\boldsymbol{x}, \boldsymbol{u}, \boldsymbol{\lambda}) = \mathcal{J}(\boldsymbol{x}, \boldsymbol{u}) + \boldsymbol{\lambda}^T R(\boldsymbol{x}, \boldsymbol{u}) \tag{22}$$

where the vector $\boldsymbol{\lambda}$ contains the Lagrangian multipliers, called adjoint variables. Since the governing equations are satisfied by definition, Eq. (22) can be differentiated with respect to $\boldsymbol{x}$:

$$\frac{d\mathcal{J}}{d\boldsymbol{x}} = \frac{d\mathcal{L}}{d\boldsymbol{x}} = \frac{\partial \mathcal{J}}{\partial \boldsymbol{x}} + \frac{\partial \mathcal{J}}{\partial \boldsymbol{u}} \frac{d\boldsymbol{u}}{d\boldsymbol{x}} + \boldsymbol{\lambda}^T \left(\frac{\partial R}{\partial \boldsymbol{x}} + \frac{\partial R}{\partial \boldsymbol{u}} \frac{d\boldsymbol{u}}{d\boldsymbol{x}} \right) \tag{23}$$

Rearranging:

$$\frac{d\mathcal{J}}{d\boldsymbol{x}} = \left(\frac{\partial \mathcal{J}}{\partial \boldsymbol{x}} + \boldsymbol{\lambda}^T \frac{\partial R}{\partial \boldsymbol{x}} \right) + \left(\frac{\partial \mathcal{J}}{\partial \boldsymbol{u}} + \boldsymbol{\lambda}^T \frac{\partial R}{\partial \boldsymbol{u}} \right) \frac{d\boldsymbol{u}}{d\boldsymbol{x}} \tag{24}$$

Since Lagrangian multipliers are arbitrary, it is possible to choose the combination that implies:

$$\frac{\partial \mathcal{J}}{\partial \boldsymbol{u}} + \boldsymbol{\lambda}^T \frac{\partial R}{\partial \boldsymbol{u}} = 0 \tag{25}$$

These are the adjoint equations. It can be seen that the dependency on the design parameters $\boldsymbol{x}$ is removed. The state variables become the known part of the problem and are used to compute the adjoint variables. Once the adjoint variable distribution in the whole domain is known, the sensitivity can be computed as:

$$\frac{d\mathcal{J}}{d\boldsymbol{x}} = \frac{\partial \mathcal{J}}{\partial \boldsymbol{x}} + \boldsymbol{\lambda}^T \frac{\partial R}{\partial \boldsymbol{x}} \tag{26}$$

In order to solve the adjoint equations expressed in Eq. (25), there are two possible methods: the discrete adjoint and the continuous adjoint. The discrete adjoint formulation discretizes the variables first, and then builds the adjoint equations. The continuous adjoint formulation builds the adjoint equations and then discretizes them. In this section the continuous adjoint equations for compressible steady RANS equations are obtained.
In order to build the continuous adjoint, it is possible to compute the gradient of $\mathcal{J}$ by expanding Eq. (22) up to the first order:

$$\delta\mathcal{L}(\boldsymbol{x}, \boldsymbol{u}, \boldsymbol{\lambda}) = \delta\mathcal{J}(\boldsymbol{x}, \boldsymbol{u}) + \boldsymbol{\lambda}^T \delta R(\boldsymbol{x}, \boldsymbol{u}) \tag{27}$$

From this expression, following the algebraic operations defined in the following sections, the adjoint equations, the associated boundary conditions and the sensitivity expression can be obtained.

B.2. Derivation of the equations

The expression of the Lagrangian, defined in Eq. (22), can be derived for the compressible case. In order to do so, first, it is necessary to define the adjoint variables:

$$\boldsymbol{\lambda} = \begin{bmatrix} \zeta \\ \boldsymbol{\chi} \\ \eta \end{bmatrix} \tag{28}$$

where ζ is the adjoint pressure, $\boldsymbol{\chi}$ is the adjoint velocity, and η is the adjoint temperature. Then, the RANS equations in their integral form are substituted into $R(\boldsymbol{x}, \boldsymbol{u})$. By defining the total energy $E_t = e + \frac{1}{2}|\boldsymbol{u}|^2$, it is possible to link the internal energy e with the temperature T through the enthalpy to obtain:

$$\begin{aligned}\mathcal{L} = \mathcal{J} &+ \int_\Omega \zeta \left(\boldsymbol{u}\cdot\nabla\rho + \rho\nabla\cdot\boldsymbol{u}\right) \mathrm{d}\Omega \\ &+ \int_\Omega \boldsymbol{\chi}\cdot\left[\rho\left(\boldsymbol{u}\cdot\nabla\boldsymbol{u}\right) + \nabla p - \nabla\cdot\boldsymbol{\tau}\right] \mathrm{d}\Omega \\ &+ \int_\Omega \eta\left[\rho C_p\left(\boldsymbol{u}\cdot\nabla T\right) - \boldsymbol{u}\cdot\nabla p - \nabla\cdot(k\nabla T) - \boldsymbol{\tau}:\nabla\boldsymbol{u}\right] \mathrm{d}\Omega\end{aligned} \tag{29}$$

From this definition of the Lagrangian, it is possible to write the variational form described in Eq. (27). Each variable is perturbed up to the first order:

$$\begin{aligned}\boldsymbol{u} &= \boldsymbol{u} + \delta\boldsymbol{u} \\ p &= p + \delta p \\ \rho &= \rho + \delta\rho \\ T &= T + \delta T \\ \boldsymbol{\tau} &= \boldsymbol{\tau} + \delta\boldsymbol{\tau}\end{aligned} \tag{30}$$

The density is linked to the pressure and the temperature through the equation of state; the viscous stress tensor is defined as directly dependent on the viscosity and the velocity. By applying the hypothesis of frozen turbulence (Schramm *et al.*, 2018), the viscosity is considered constant and $\delta\mu = 0$. Therefore, $\delta\boldsymbol{\tau}$ can be linked to $\delta\boldsymbol{u}$:

$$\begin{aligned}\delta\boldsymbol{\tau} &= \mu\left(\nabla\delta\boldsymbol{u} + (\nabla\delta\boldsymbol{u})^T - \frac{2}{3}(\nabla\cdot\delta\boldsymbol{u})\boldsymbol{I}\right) \\ \delta\rho &= \left(\frac{1}{RT}\right)\delta p + \left(-\frac{\rho}{T}\right)\delta T\end{aligned} \tag{31}$$

In order to obtain $\delta\mathcal{L}$, the variational terms are factored out of the differential operators. This is achieved through the application of the divergence theorem, which moves the derivatives from the variational terms to the adjoint variables:

$$\int_\Omega \nabla\cdot\boldsymbol{v}\mathrm{d}\Omega = \int_{\partial\Omega} \boldsymbol{v}\cdot\boldsymbol{n}\,\mathrm{d}S \tag{32}$$

This causes the boundary integrals to appear. After the manipulations just described, Eq. (29) becomes:

$$\begin{aligned}\delta\mathcal{L} = \delta\mathcal{J} &+ \int_{\partial\Omega} \delta\boldsymbol{u}\cdot\left[\zeta\rho\boldsymbol{n} + (\rho\boldsymbol{u}\cdot\boldsymbol{n})\boldsymbol{\chi} + \rho(\boldsymbol{u}\cdot\boldsymbol{\chi})\cdot\boldsymbol{n} - \eta\boldsymbol{\tau}\cdot\boldsymbol{n} + \mu\boldsymbol{\tau}^*\cdot\boldsymbol{n}\right] \mathrm{d}S \\ &+ \int_{\partial\Omega} \delta p\left[\left(\frac{1}{RT}\right)\zeta\boldsymbol{u}\cdot\boldsymbol{n} + \boldsymbol{\chi}\cdot\boldsymbol{n} - \eta(\boldsymbol{u}\cdot\boldsymbol{n})\right] \mathrm{d}S + \int_{\partial\Omega} \delta T\left[\eta\rho C_p\boldsymbol{u}\cdot\boldsymbol{n} + k(\nabla\eta\cdot\boldsymbol{n}) - \left(\frac{\rho}{T}\right)\zeta\boldsymbol{u}\cdot\boldsymbol{n}\right] \mathrm{d}S \\ &+ \int_{\partial\Omega} -\left[\mu\left(\nabla\delta\boldsymbol{u} + (\nabla\delta\boldsymbol{u})^T - \frac{2}{3}(\nabla\cdot\delta\boldsymbol{u})\boldsymbol{I}\right)\right]\cdot\boldsymbol{\chi}\cdot\boldsymbol{n}\,\mathrm{d}S + \int_{\partial\Omega} -\eta k\nabla\delta T\cdot\boldsymbol{n}\mathrm{d}S \\ &+ \int_\Omega \delta\boldsymbol{u}\cdot\left[-\rho\nabla\zeta - \boldsymbol{\chi}\nabla\cdot(\rho\boldsymbol{u}) - \rho\boldsymbol{u}\cdot\nabla\boldsymbol{\chi} - \rho(\nabla\boldsymbol{\chi})^T\boldsymbol{u} + \eta\rho C_p\nabla T - \eta\nabla p + \nabla\cdot(\eta\boldsymbol{\tau}) - \mu(\nabla\cdot\boldsymbol{\tau}^*)\right]\mathrm{d}\Omega \\ &+ \int_\Omega \delta p\Big[-\nabla\cdot\boldsymbol{\chi} + \nabla\cdot(\eta\boldsymbol{u}) + \left(\frac{1}{RT}\right)\left[-\boldsymbol{u}\cdot\nabla\zeta + \boldsymbol{\chi}\cdot(\boldsymbol{u}\cdot\nabla\boldsymbol{u}) + \eta C_p(\boldsymbol{u}\cdot\nabla T)\right]\Big] \mathrm{d}\Omega \\ &+ \int_\Omega -\delta T\left[\nabla\cdot(\eta\rho C_p\boldsymbol{u}) + \nabla\cdot(k\nabla\eta) + \left(\frac{\rho}{T}\right)\left[-\boldsymbol{u}\cdot\nabla\zeta + \boldsymbol{\chi}\cdot(\boldsymbol{u}\cdot\nabla\boldsymbol{u}) + \eta C_p(\boldsymbol{u}\cdot\nabla T)\right]\right] \mathrm{d}\Omega\end{aligned} \tag{33}$$

where $\boldsymbol{\tau}^*$ is the operator with the same structure as $\boldsymbol{\tau}$, but which acts on the adjoint variables:

$$\boldsymbol{\tau}^* = (\nabla\boldsymbol{\chi} - \eta\nabla\boldsymbol{u}) + (\nabla\boldsymbol{\chi} - \eta\nabla\boldsymbol{u})^T - \frac{2}{3}(\nabla\cdot(\nabla\boldsymbol{\chi} - \eta\nabla\boldsymbol{u}))\boldsymbol{I} \tag{34}$$

At this point, in order to completely determine $\delta\mathcal{L}$, the target function needs to be defined. Eq.(20) relates the sensitivity of the final quantity of interest, the lift-to-drag ratio, to the sensitivities of lift and drag. Hence, these quantities are the selected target functions and can be defined in integral form as:

$$\begin{aligned}D &= \int_{S_a} p(-\boldsymbol{n})\cdot\hat{\boldsymbol{i}}\,\mathrm{d}S + \int_{S_a} (\boldsymbol{\tau}\cdot\boldsymbol{n})\cdot\hat{\boldsymbol{i}}\,\mathrm{d}S \\ L &= \int_{S_a} p(-\boldsymbol{n})\cdot\hat{\boldsymbol{j}}\,\mathrm{d}S + \int_{S_a} (\boldsymbol{\tau}\cdot\boldsymbol{n})\cdot\hat{\boldsymbol{j}}\,\mathrm{d}S\end{aligned} \tag{35}$$

where S_a is the airfoil surface and $\boldsymbol{n}$ is the airfoil normal.
The mathematical approach to obtain the adjoint equations and boundary conditions will be presented using drag as the objective function. To obtain the sensitivity of the lift, the same algebraic steps need to be performed and the results expressed in Eq.(18) are obtained.
Defining $\delta\mathcal{J} = \delta D$:

$$\delta\mathcal{J} = \int_{S_a} \delta p(-\boldsymbol{n}) \cdot \hat{\boldsymbol{i}}\, \mathrm{d}S + \int_{S_a} (\delta\boldsymbol{\tau} \cdot \boldsymbol{n}) \cdot \hat{\boldsymbol{i}}\, \mathrm{d}S \tag{36}$$

Following the procedure described by Ohashi *et al.* (2021), the domain boundary $\partial\Omega$ can be decomposed into the airfoil surface S_a and the farfield boundary S_Ω. Similarly, it is possible to split the variables (p, $\boldsymbol{u}$, T) in two. The surface variables (p_S, $\boldsymbol{u}_S$, T_S) are evaluated at the airfoil surface and are zero everywhere else; these represent the control variables for this application. The domain variables (p_Ω, $\boldsymbol{u}_\Omega$, T_Ω) are the variables within the domain and are zero on S_a.
As expressed in Eq. (25), in order to obtain the adjoint equations, the derivative of the Lagrangian with respect to the state variables needs to be set to zero. In the variational case, this operator is represented by the terms dependent on (p_Ω, $\boldsymbol{u}_\Omega$, T_Ω). Since (p_Ω, $\boldsymbol{u}_\Omega$, T_Ω) are zero on the airfoil surface, the surface integrals that depend on these variables will also be zero if evaluated on the airfoil surface. The only surface integral defined on S_a that survives is the one containing $\nabla\boldsymbol{u}_\Omega$ because, while $\boldsymbol{u}_\Omega$ is zero at the wall, its gradient is non-zero. Starting from Eq. (33), the expression in Eq. (36) is substituted; the variable splitting just described is applied, and the adjoint equations and the corresponding boundary conditions are obtained by setting the terms depending on p_Ω, $\boldsymbol{u}_\Omega$ or T_Ω, reported below, to zero:

$$\begin{aligned}
&\int_\Omega \delta\boldsymbol{u}_\Omega \cdot [-\rho\nabla\zeta - \rho\boldsymbol{u}\cdot\nabla\boldsymbol{\chi} - \rho(\nabla\boldsymbol{\chi})^T\boldsymbol{u} + \eta\rho C_p\nabla T - \eta\nabla p + \nabla\cdot(\eta\boldsymbol{\tau}) - \mu(\nabla\cdot\boldsymbol{\tau}^*)]\,\mathrm{d}\Omega \\
&+ \int_\Omega \delta p_\Omega \left[-\nabla\cdot\boldsymbol{\chi} + \nabla\cdot(\eta\boldsymbol{u}) + \left(\frac{1}{RT}\right)[-\boldsymbol{u}\cdot\nabla\zeta + \boldsymbol{\chi}\cdot(\boldsymbol{u}\cdot\nabla\boldsymbol{u}) + \eta C_p(\boldsymbol{u}\cdot\nabla T)] \right] \mathrm{d}\Omega \\
&+ \int_\Omega -\delta T_\Omega \left[C_p\rho\boldsymbol{u}\cdot\nabla\eta + \nabla\cdot(k\nabla\eta) + \left(\frac{\rho}{T}\right)[-\boldsymbol{u}\cdot\nabla\zeta + \boldsymbol{\chi}\cdot(\boldsymbol{u}\cdot\nabla\boldsymbol{u}) + \eta C_p(\boldsymbol{u}\cdot\nabla T)] \right] \mathrm{d}\Omega \\
&+ \int_{S_\Omega} \delta\boldsymbol{u}_\Omega \cdot [\zeta\rho\boldsymbol{n} + (\rho\boldsymbol{u}\cdot\boldsymbol{n})\boldsymbol{\chi} + \rho(\boldsymbol{u}\cdot\boldsymbol{\chi})\cdot\boldsymbol{n} - \eta\boldsymbol{\tau}\cdot\boldsymbol{n} + \mu\boldsymbol{\tau}^*\cdot\boldsymbol{n}]\,\mathrm{d}S \\
&+ \int_{S_\Omega} \delta p_\Omega \left[\left(\frac{1}{RT}\right)\zeta\boldsymbol{u}\cdot\boldsymbol{n} + \boldsymbol{\chi}\cdot\boldsymbol{n} - \eta(\boldsymbol{u}\cdot\boldsymbol{n}) \right] \mathrm{d}S + \int_{S_\Omega} -\eta k\nabla\delta T_\Omega\cdot\boldsymbol{n}\,\mathrm{d}S \\
&+ \int_{S_\Omega} \delta T_\Omega \left[\eta\rho C_p\boldsymbol{u}\cdot\boldsymbol{n} + k(\nabla\eta\cdot\boldsymbol{n}) - \left(\frac{\rho}{T}\right)\zeta\boldsymbol{u}\cdot\boldsymbol{n} \right] \mathrm{d}S \\
&+ \int_{S_\Omega} -\left[\mu\left(\nabla\delta\boldsymbol{u}_\Omega + (\nabla\delta\boldsymbol{u}_\Omega)^T - \frac{2}{3}(\nabla\cdot\delta\boldsymbol{u}_\Omega)\boldsymbol{I} \right) \right] \cdot\boldsymbol{\chi}\cdot\boldsymbol{n}\,\mathrm{d}S \\
&+ \int_{S_a} -\left[\mu\left(\nabla\delta\boldsymbol{u}_\Omega + (\nabla\delta\boldsymbol{u}_\Omega)^T - \frac{2}{3}(\nabla\cdot\delta\boldsymbol{u}_\Omega)\boldsymbol{I} \right) \right] \cdot\boldsymbol{\chi}\cdot\boldsymbol{n}\,\mathrm{d}S \\
&+ \int_{S_a} \left[\mu\left(\nabla\delta\boldsymbol{u}_\Omega + (\nabla\delta\boldsymbol{u}_\Omega)^T - \frac{2}{3}(\nabla\cdot\delta\boldsymbol{u}_\Omega)\boldsymbol{I} \right) \right] \cdot\hat{\boldsymbol{i}}\cdot\boldsymbol{n}\,\mathrm{d}S = 0
\end{aligned} \tag{37}$$

The adjoint equations, expressed in Eq. (17), are obtained by setting to zero the volume integrals. Since the variational terms are arbitrary, the only possibility is that the integrands are identically zero.
Boundary conditions are set in order to make the boundary integrals vanish. Such conditions are strictly related to the constraints adopted for the state variables in the original simulation. A standard transonic, compressible simulation sets the boundary values of the variables as presented in Table 6.

Table 6: Typical boundary conditions of a transonic simulation in OpenFOAM

	Inlet	Outlet	Airfoil Surface
p	Fixed Value	Wave Transmissive	Zero Gradient
$\boldsymbol{u}$	Fixed Value	Zero Gradient	No-Slip
T	Fixed Value	Zero Gradient	Zero Gradient

Boundary conditions that prescribe the value of a variable at the boundary (fixed-value and no-slip) do not allow variations of the quantities on which they act. The zero-gradient type sets the normal gradient of a given quantity to zero, but allows variations of the quantity itself. The adjoint counterpart of this last condition is formulated in order to make the integrals depending on the variational terms vanish, since the boundary terms

depending on the gradient of the variations are zero. If a quantity has a fixed-value constraint in the primal simulation, the variational term of that quantity is zero and the corresponding surface integrals are always zero. The associated adjoint boundary conditions are imposed to make the other surface integrals, which depend on the gradient of the variation, vanish.
By splitting integrals over S_Ω into inlet and outlet contributions, the boundary conditions for the adjoint variables are derived and summarized in Table 4.
It is worth noting that OpenFOAM allows the user to use mixed boundary conditions, which automatically switch between fixed value and zero gradient, depending on whether the boundary experiences inflow or outflow. If an adjoint solver for a baseline simulation that enforces these conditions is developed, the constraints need to switch between the condition imposed for fixed value and the one imposed for zero gradient following the same logic.

B.3. Computation of the sensitivity

Once the adjoint equations are solved, the adjoint variables are known over the entire domain. Hence, it is possible to obtain the value of the sensitivity of the objective function to the control parameters. In Eq. (37), all the terms depending on p_Ω, $\boldsymbol{u}_\Omega$ and T_Ω are set to zero to derive the adjoint equations and their boundary conditions; the sensitivity is computed from the remaining terms in the equation since $\delta\mathcal{L} = \delta\mathcal{J}$. Considering the constraints imposed at the airfoil, the following expression is obtained:

$$\begin{aligned}\delta\mathcal{J} = &\int_{S_a} \delta\boldsymbol{u}_S \cdot [\zeta\rho\boldsymbol{n} + (\rho\boldsymbol{u}\cdot\boldsymbol{n})\boldsymbol{\chi} + \rho(\boldsymbol{u}\cdot\boldsymbol{\chi})\cdot\boldsymbol{n} - \eta\boldsymbol{\tau}\cdot\boldsymbol{n} + \mu\boldsymbol{\tau}^*\cdot\boldsymbol{n}]\,\mathrm{d}S \\ &+ \int_{S_a} \delta p_S \left[\left(\frac{1}{RT}\right)\zeta\boldsymbol{u}\cdot\boldsymbol{n} - \eta(\boldsymbol{u}\cdot\boldsymbol{n})\right]\mathrm{d}S \\ &+ \int_{S_a} \delta T_S \left[\eta\rho C_p\boldsymbol{u}\cdot\boldsymbol{n} + k(\nabla\eta\cdot\boldsymbol{n}) - \left(\frac{\rho}{T}\right)\zeta\boldsymbol{u}\cdot\boldsymbol{n}\right]\mathrm{d}S\end{aligned} \tag{38}$$

In each configuration considered in this study, the velocity at the wall is either zero or purely tangential to the surface, so it is possible to write $\boldsymbol{u}\cdot\boldsymbol{n} = 0$. Considering the boundary conditions expressed in Table 4, also $\nabla\eta\cdot\boldsymbol{n} = \frac{\partial\eta}{\partial\boldsymbol{n}} = 0$ and the term described in Eq. (38) leads to the sensitivity functions described in Eq. (18) and Eq. (19). Once such quantities are computed, the sensitivity of the lift-to-drag ratio to the application of a slip length at the wall can be computed as described in Eq. (20).

Abstract in lingua italiana

Questa tesi studia l'effetto della posizione di applicazione di riblets su un profilo alare transonico tramite la risoluzione di RANS. La sensibilità delle prestazioni del profilo, espresse in termini di efficienza aerodinamica, rispetto alla posizione di applicazione del controllo è valutata attraverso uno studio parametrico. L'effetto di riblets localmente ottimali è implementato in un solutore RANS imponendo uno slip parziale a parete tramite un'opportuna condizione al contorno per la velocità. Coerentemente con la letteratura, i risultati confermano che la presenza di riblets riduce l'attrito superficiale e modifica le caratteristiche del flusso, spostando l'onda d'urto verso il bordo d'uscita. Il dorso si dimostra essere la parte più sensibile all'applicazione del controllo: le configurazioni con le prestazioni migliori sono quelle situate nella parte anteriore che causano le maggiori alterazioni del flusso intorno al profilo. Estendendo l'analisi a due diversi numeri di Reynolds, si osserva che l'efficacia del controllo si riduce all'aumentare di tale parametro. A $\mathrm{Re}_\infty = 3 \cdot 10^5$, il profilo interamente coperto di riblets registra un incremento di efficienza pari a $\Delta E = +7.4\%$, mentre la migliore configurazione a copertura parziale raggiunge un $\Delta E = +1.9\%$. A $\mathrm{Re}_\infty = 10^6$, questi valori scendono rispettivamente a $\Delta E = +4.0\%$ per il profilo completamente controllato e a $\Delta E = +1.7\%$ per la configurazione a copertura parziale ottima. Infine sono derivate le equazioni aggiunte necessarie per ricavare la sensibilità dell'efficienza all'imposizione di una velocità di slip a parete, stabilendo così le fondamenta teoriche per un futuro processo di ottimizzazione completamente automatizzato.

Parole chiave: RANS, Riduzione dell'attrito, Flussi Transonici